Stem Cell Reports
Article

OPEN ACCESS

PSEN1 Mutant iPSC-Derived Model Reveals Severe Astrocyte Pathology in Alzheimer's Disease

Minna Oksanen,[1] Andrew J. Petersen,[2] Nikolay Naumenko,[1] Katja Puttonen,[1] Šárka Lehtonen,[1] Max Gubert Olivé,[1] Anastasia Shakirzyanova,[1] Stina Leskelä,[1] Timo Sarajärvi,[3] Matti Viitanen,[4,9] Juha O. Rinne,[5,6] Mikko Hiltunen,[3,7] Annakaisa Haapasalo,[1] Rashid Giniatullin,[1] Pasi Tavi,[1] Su-Chun Zhang,[2,8] Katja M. Kanninen,[1] Riikka H. Hämäläinen,[1] and Jari Koistinaho[1,*]

[1]A.I.Virtanen Institute for Molecular Sciences, University of Eastern Finland, 70210 Kuopio, Finland
[2]Waisman Center, University of Wisconsin, Madison, WI 53705, USA
[3]Institute of Biomedicine, University of Eastern Finland, 70210 Kuopio, Finland
[4]Department of Geriatrics, University of Turku, Turku City Hospital, 20700 Turku, Finland
[5]Turku PET Centre, University of Turku, 20700 Turku, Finland
[6]Division of Clinical Neurosciences, Turku University Hospital, 20700 Turku, Finland
[7]Department of Neurology, Kuopio University Hospital, 70210 Kuopio, Finland
[8]Departments of Neuroscience and Neurology, University of Wisconsin, Madison, WI 53705, USA
[9]Department of Geriatrics, Karolinska Institutet and Karolinska University Hospital, Huddinge, 14186 Stockholm, Sweden
*Correspondence: jari.koistinaho@uef.fi
https://doi.org/10.1016/j.stemcr.2017.10.016

SUMMARY

Alzheimer's disease (AD) is a common neurodegenerative disorder and the leading cause of cognitive impairment. Due to insufficient understanding of the disease mechanisms, there are no efficient therapies for AD. Most studies have focused on neuronal cells, but astrocytes have also been suggested to contribute to AD pathology. We describe here the generation of functional astrocytes from induced pluripotent stem cells (iPSCs) derived from AD patients with *PSEN1 ΔE9* mutation, as well as healthy and gene-corrected isogenic controls. AD astrocytes manifest hallmarks of disease pathology, including increased β-amyloid production, altered cytokine release, and dysregulated Ca^{2+} homeostasis. Furthermore, due to altered metabolism, AD astrocytes show increased oxidative stress and reduced lactate secretion, as well as compromised neuronal supportive function, as evidenced by altering Ca^{2+} transients in healthy neurons. Our results reveal an important role for astrocytes in AD pathology and highlight the strength of iPSC-derived models for brain diseases.

INTRODUCTION

Alzheimer's disease (AD) is a common dementing disorder characterized by progressive decline of cognitive functions, especially memory loss. The neuropathology of AD includes extracellular deposits of β-amyloid (Aβ) in senile plaques, intracellular neurofibrillary tangles comprising hyperphosphorylated tau, synaptic dysfunction, and neuronal death (Blennow et al., 2006). While most AD cases are sporadic late-onset type (LOAD), 1%–2% of the cases are of a familial early-onset type AD (EOAD), with underlying mutations in presenilin-1 and -2 (*PSEN1/2*) or amyloid precursor protein (*APP*) genes (Waring and Rosenberg, 2008). Neuropathological changes and apparent cellular dysfunctions are similar in various forms of LOAD and EOAD, but the exact mechanisms underlying the onset and progression of AD are not well understood. According to the largely accepted amyloid cascade hypothesis, the extracellular accumulation of Aβ peptides triggers the onset of AD (Hardy and Selkoe, 2002). Although considerable pre-clinical and clinical evidence supports the amyloid cascade model, all experimental therapies built on this hypothesis have thus far been unsuccessful in clinics (Castello et al., 2014; Golde et al., 2011). Several factors have probably contributed to the failures in AD drug development, including unsuitable pre-clinical research models, such as transgenic mice or human tumor-derived cell lines, which do not fully recapitulate the human disease. Recent cellular models created from patient cells using induced pluripotent stem cell (iPSC) technology have provided promising tools for understanding human disease mechanisms. So far, most of the human iPSC (hiPSC)-based AD models have concentrated on hippocampal or cortical neurons (Kondo et al., 2013; Nieweg et al., 2015), but other cell types of the CNS are also likely to contribute to AD pathology.

Astrocytes are the most abundant non-neuronal cell type in the CNS and have multiple indispensable tasks in brain development and function, including energy supply to neurons in the form of lactate, as well as synapse formation and maintenance (Belanger et al., 2011; Oberheim et al., 2006). Human astrocytes are about 20 times larger, integrate 20 times more synapses, and propagate Ca^{2+} waves far more quickly than their rodent counterparts (Oberheim et al., 2009). Moreover, the greatest genetic difference between human and rodent brain has been identified to be in glial transcripts (Zhang et al., 2016). As astrocytes have been suggested to have a role in AD pathogenesis (Vincent et al., 2010), we generated hiPSC-derived astrocytes from patients with EOAD carrying *PSEN1* exon 9 deletion

Table 1. Summary of the Healthy Controls and Patients Used in This Study

Patient	Sex	Age When Sample Taken (Years)	*PSEN1* Genotype	*APOE* Genotype	Status	Sample Type	Isogenic Control Line
Ctrl1	F	adult	normal	ε3/ε3	normal	skin biopsy	–
Ctrl2	M	62	normal	ε3/ε3	normal	skin biopsy	–
Ctrl3	F	44	normal	ε3/ε3	normal	skin biopsy	–
AD1	F	64	ΔE9	ε3/ε3	Alzheimer's disease	blood sample	–
AD2	M	48	ΔE9	ε3/ε3	Alzheimer's disease	skin biopsy	*PSEN1* ΔE9 corrected
AD3	F	47	ΔE9	ε3/ε3	pre-symptomatic	skin biopsy	*PSEN1* ΔE9 corrected

See also Table S1; Figures S1 and S2.

(4.6 kb deletion; the Finnish *PSEN1 ΔE9*) (Crook et al., 1998) and report here that astrocytes manifest many hallmarks of AD pathology. Our findings highlight the importance of astrocytes in AD pathology and demonstrate that hiPSC-derived astrocytes provide a valuable tool for studying AD disease mechanisms.

RESULTS

Patient and Control Cells

iPSC lines were generated from three individuals carrying the *PSEN1 ΔE9* mutation, two diagnosed with AD and one pre-symptomatic with no clinical diagnosis, and from three healthy adult control individuals (Table 1). All six individuals carried the neutral *ε3/ε3* isoforms of *APOE*, the most important risk gene for LOAD. To examine the cause-effect relationship between *ΔE9* mutation and AD phenotype, we also generated gene-corrected isogenic control lines from one symptomatic AD patient and the pre-symptomatic *PSEN1 ΔE9* carrier using a previously published donor plasmid-mediated CRISPR/Cas9 workflow (Figure S1 and Table 1) (Chen et al., 2015). After 10 passages, all iPSC lines showed typical morphological characteristics of pluripotent stem cells as well as high expression of pluripotency markers (Figures S2A and S2B; Table S1). All the studied lines formed embryoid bodies, differentiated spontaneously toward the three germ layers, and presented normal euploid karyotypes (Figures S2C–S2F and Table S1). Insertion of the exon 9 in the isogenic control lines was confirmed by PCR amplifications of the targeted area (Figures S1D–S1F) and Sanger sequencing across the deletion breakpoints (data not shown).

iPSCs Efficiently Differentiate into Functional Astrocytes

Astrocyte differentiation was carried out by a slightly modified protocol from Krencik et al. (2011) (Figure 1A). Ciliary neurotrophic factor (CNTF) and bone morphogenetic protein 4 (BMP4) were applied in the final maturation stage, as they have been shown to promote the generation of bona fide astrocytes (Magistri et al., 2016). The mRNA expression of *GFAP* increased gradually to about 100-fold from 1-month-old to 6-month-old spheres, and further by 20-fold when maturating the dissociated cells for 7 days (Figure 1B). At the age of 6 months, no TUJ1-immunoreactive neuronal cells were observed in the dissociated sphere cultures (Figure 1C). Finally, more than 90% of the cells were GFAP and/or S100β positive, acquiring a stellate morphology, after maturation with CNTF and BMP4 (Figure 1D). The mRNA expression levels of *GFAP* and *S100B* were significantly higher when compared with iPSC-derived neurons from the same lines (Figure 1E). The matured astrocytes from all the lines, independent of the disease status, showed also other typical characteristics, such as high mRNA expression of the astrocyte-specific glutamate transporters *SLC1A2* and *SLC1A3*, and water channel *AQP4* (Figure 1F) in comparison with neurons. Cells were able to take up glucose, produce and secrete cytokines and glutathione, and propagate intercellular Ca^{2+} waves (Figures 1G–1I and S3A). No evident differences were seen in the differentiation potential between the genotypes, and both AD and control iPSCs generated comparable, functional astrocytes.

PSEN1 ΔE9 Mutant Astrocytes Contribute to β-Amyloid Pathology

Wild-type presenilin-1 (PS-1) is initially translated as a 43-kDa molecule, which is processed to stable N-terminal (NTF) and C-terminal fragments (CTF) of 27 kDa and 17 kDa, respectively (Thinakaran et al., 1996). PS-1 NTFs and CTFs are critically involved in composing the active γ-secretase complex. Since *PSEN1 ΔE9* mutation leads to an in-frame deletion of the endoproteolytic site and consequently to the accumulation of uncleaved PS-1 of a smaller molecular weight (~40 kDa) as compared with the

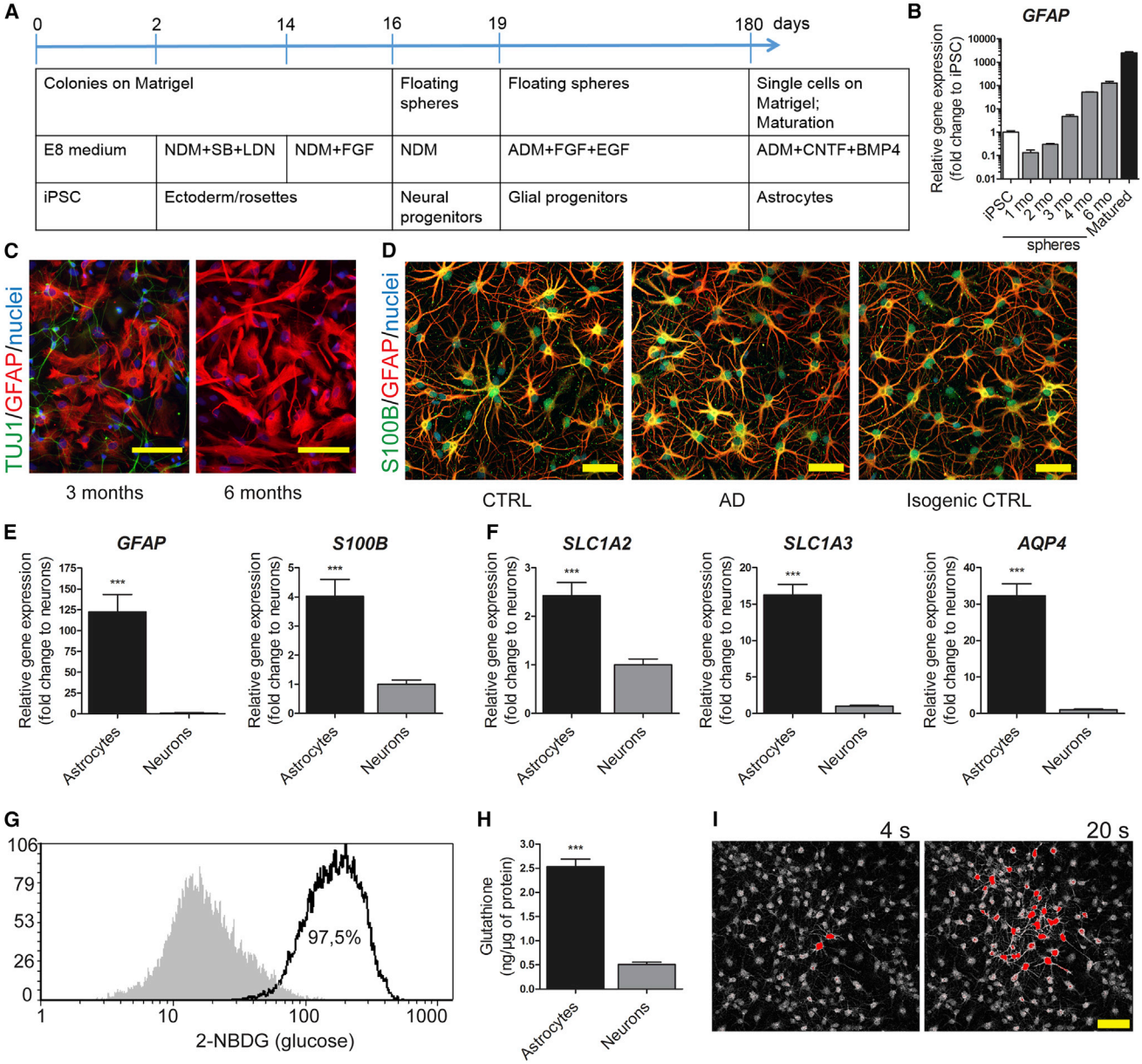

Figure 1. Differentiation and Characterization of iPSC-Derived Astrocytes

(A) Schematic illustrating the astrocyte differentiation protocol. NDM, neural differentiation medium; SB, SB431542; LDN, LDN193189; ADM, astrocyte differentiation medium.

(B) Relative gene expression of *GFAP* during astrocytic differentiation shown as fold change to iPSCs. Representative data from three independent differentiations.

(C) Representative immunocytochemistry images of cells dissociated from 3- or 6-month-old spheres stained for TUJ1 (green) and GFAP (red). Nuclei are stained with Hoechst. Scale bars, 100 µm.

(D) Representative immunocytochemistry images of astrocytes from control, AD, and isogenic control lines matured with CNTF and BMP4 for 7 days, stained for S100β (green) and GFAP (red). Nuclei are stained with Hoechst. Scale bars, 50 µm.

(E) Relative gene expression levels of *GFAP* and *S100B* in astrocytes shown as fold change to iPSC-derived neurons (astrocytes, n = 14 lines; neurons, n = 5 lines; ***p < 0.001).

(F) Relative gene expression levels of *SLC1A2*, *SLC1A3*, and *AQP4* in astrocytes shown as fold change to iPSC-derived neurons (astrocytes, n = 14 lines; neurons, n = 5 lines; ***p < 0.001).

(legend continued on next page)

wild-type PS-1 (Thinakaran et al., 1996), we analyzed PS-1 endoproteolytic cleavage. As expected, *PSEN1 ΔE9* mutant astrocytes showed robust accumulation of full-length PS-1, which was undetectable in control cells, and subsequent reduction in CTFs (Figures 2A and 2B). However, we did not observe differences in the enzymatic activity of γ-secretase (Figure 2G), nor at the protein expression level of APP (Figures 2A and 2C). Neurons have been thought to be the main source of Aβ production, but astrocytes are also able to secrete Aβ (Liao et al., 2016). Thus, we quantified Aβ1–40 and Aβ1–42 from the astrocyte culture media. The secretion of Aβ1–42 was increased about 5-fold in the AD cultures when compared with the controls, whereas Aβ1–40 secretion was not altered (Figures 2D, 2E, S4A, and S4B). This led to a significantly increased Aβ1–42/Aβ1–40 ratio and toxic Aβ profile in AD astrocytes (Figures 2F and S4C). Treatment with the γ-secretase inhibitor DAPT decreased the production of Aβ1–40 and completely blocked the production of Aβ1–42 in both AD and control astrocytes (Figures 2D and 2E). The overall Aβ production by astrocytes was comparable with that of iPSC-derived neurons from the same lines (Figures S4D and S4E), and the mRNA expression levels of *APP* and *BACE1* were only slightly lower in astrocytes when compared with neurons (Figures S4G and S4H), highlighting the importance of astrocytes as Aβ-producing cells. Importantly, both the PS-1 endoproteolytic processing and Aβ secretion were resolved in the isogenic control lines (Figure 2), verifying that the partial correction of the deletion had restored PS-1 function. We next measured the astrocytic uptake of Aβ1–42 by fluorescence-activated cell sorting (FACS). After 16 hr of incubation with a fluorochrome-conjugated fibrilized Aβ1–42, internalized Aβ was quantified and AD astrocytes showed reduced capacity to take up Aβ when compared with controls (Figure 2H). These results show that *PSEN1 ΔE9* astrocytes present the endoproteolytic defect typical for this specific AD mutation and that AD astrocytes may contribute to amyloid pathology by both increased release and compromised uptake of Aβ1–42.

Ca^{2+} Signaling in the ER Is Disturbed in *PSEN1 ΔE9* Mutant Astrocytes

Several *PSEN1* mutations, including *PSEN1 ΔE9*, have been reported to disturb Ca^{2+} release from the ER (Cedazo-Minguez et al., 2002; Ito et al., 1994). Thus, we next analyzed ER Ca^{2+} cycling and especially Ca^{2+} leakage from the ER. The non-specific Ca^{2+} leakage was studied by simultaneous blocking of ryanodine receptor (RyR), inositol triphosphate receptor (IP_3R), and SERCA (Figure 3A). The rate of the non-specific Ca^{2+} release, represented by the slope of the increase in $[Ca^{2+}]_i$ level, was faster in AD than in control astrocytes (Figures 3B and S5). These results show that *PSEN1 ΔE9* AD astrocytes manifest altered cellular Ca^{2+} homeostasis.

Cytokine Secretion after Inflammatory Stimulation Is Altered in *PSEN1 ΔE9* Mutant Astrocytes

Given that astrocytes contribute to neuroinflammation in AD (Heneka et al., 2015), we analyzed the cytokine secretion profile following pro-inflammatory stimulation. The optimal stimulation was determined by comparing two key pro-inflammatory mediators increased in AD brain, interleukin-1β (IL-1β) (10 ng/mL) and tumor necrosis factor α (TNFα) (50 ng/mL). Stimulation of control astrocytes with IL-1β and/or TNFα for 48 hr led to increased cytokine secretion to media (Figure S3A). Concomitantly, the expression of inflammation-related genes *IL1B*, *IL6*, *IL10*, *TNF*, *CCL5*, and *NOS2* was upregulated after stimulation (Figure S3B). Importantly, stimulation with lipopolysaccharide had no effect (Figures S3A and S3B), which is in line with the previous knowledge on human astrocytes and further validates the identity of our cells (Tarassishin et al., 2014). We next treated astrocytes with a combination of IL-1β and TNFα and compared the cytokine secretion between AD and control cells. Upon inflammatory stimulation, *PSEN1 ΔE9* astrocytes secreted significantly higher levels of IL-2, IL-6, IL-10, and granulocyte macrophage colony-stimulating factor (GM-CSF) than control astrocytes, whereas secretion of CCL5 was lower in the *PSEN1 ΔE9* cultures (Figure 4). Interestingly, treatment with γ-secretase inhibitor DAPT led to significant reduction in IL-2 and GM-CSF secretion from AD astrocytes while it had no effect on control cells (Figure 4). These data suggest that the altered cytokine secretion profile of astrocytes may enhance neuroinflammation in AD.

Altered Metabolism in *PSEN1 ΔE9* Mutant Astrocytes Leads to Increased ROS and Reduced Lactate Production

We next analyzed the metabolic activity of the cells by measuring oxygen consumption rate (OCR) and extracellular acidification rate (ECAR) by Seahorse XF Technology

(G) Representative FACS histogram of glucose uptake analyzed by fluorescent glucose analog. Gray area shows untreated cells and the black line shows cells incubated with 2-NBDG; 97.5% of the cells were positive for 2-NBDG after 30 min of incubation.
(H) Glutathione secreted to media (astrocytes, n = 14 lines; neurons, n = 5 lines; ***p < 0.001).
(I) Propagation of intercellular calcium waves. Representative images of Fluo4-loaded cells are shown 4 and 20 s after electrical stimulation. Scale bar, 50 μm.
All data are presented as mean ± SEM. See also Figures S1–S3.

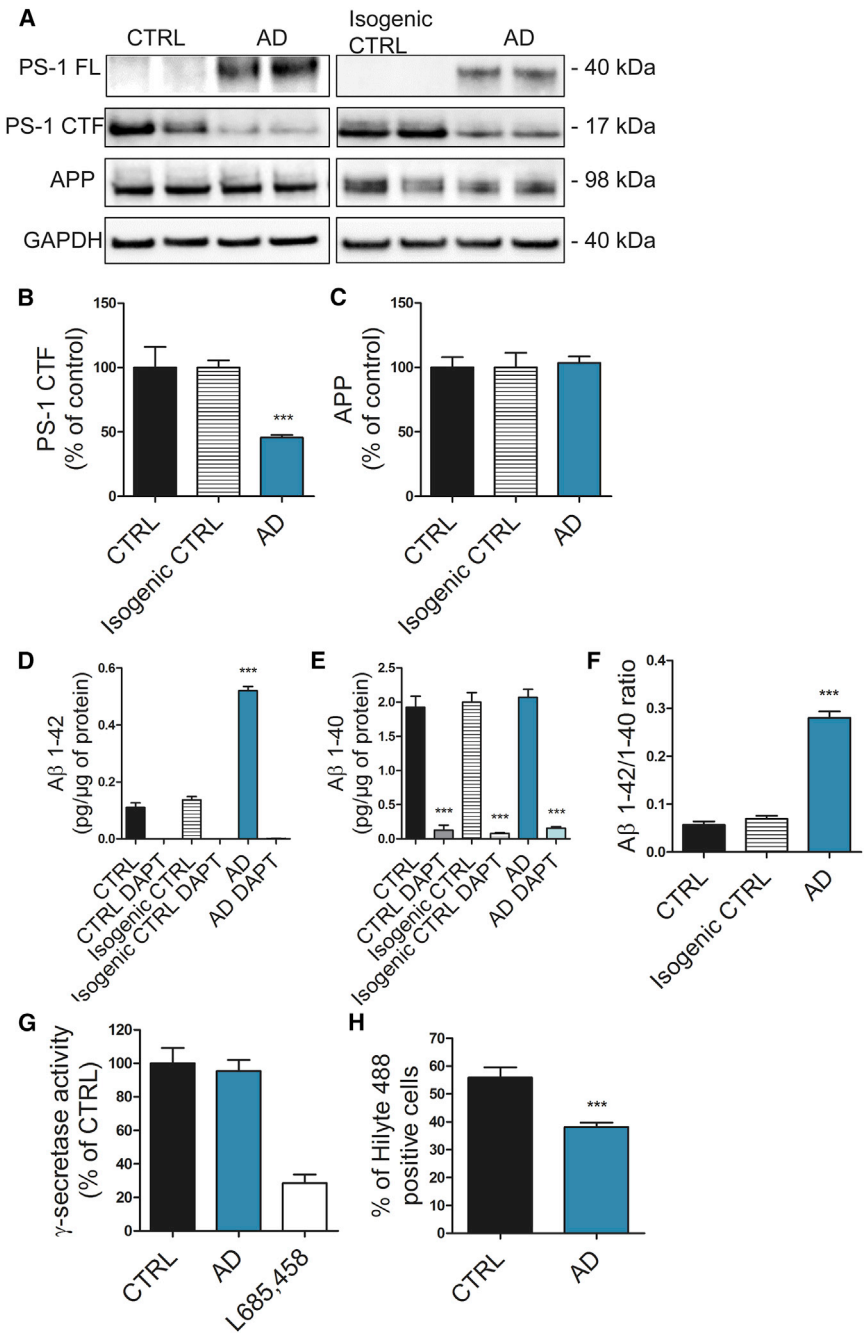

Figure 2. AD Astrocytes Present Hallmarks of β-Amyloid Pathology

(A) Representative western blot images of the endoproteolysis of PS-1 in astrocytes. PS-1 FL was not detected in control and isogenic control samples. GAPDH was used as loading control. PS-1 FL, full-length PS-1; PS-1 CTF, C-terminal fragment of PS-1.

(B and C) Quantification of PS-1 CTF (B) and APP (C) levels. Results normalized against GAPDH and shown as percentage of control (CTRL, n = 6 lines; isogenic CTRL, n = 4 replicates from 2 lines; AD, n = 6 lines; ***p < 0.001).

(D–F) Aβ1–42 (D), Aβ1–40 (E), and Aβ1–42/1–40 ratio (F) were quantified from media with or without γ-secretase inhibitor DAPT and normalized to total protein content. Three independent experiments (CTRL, n = 6 lines; isogenic CTRL, n = 4 replicates from 2 lines; AD, n = 6 lines; ***p < 0.001).

(G) γ-Secretase activity shown as percentage of control. γ-Secretase inhibitor L685,458 was added to validate the assay (CTRL, n = 6 lines; AD, n = 6 lines; GSI-treated, n = 2 lines).

(H) Percentage of cells positive for HiLyte 488-labeled Aβ1–42 representing Aβ uptake quantified by FACS. Three independent experiments (CTRL, n = 6 lines; AD, n = 6 lines; ***p < 0.001).

All data are presented as mean ± SEM. See also Figures S1 and S4.

(Figures 5A and 5B). Interestingly, *PSEN1 ΔE9* astrocytes were more oxidative than isogenic control cells, which relied more on glycolysis as typical for astrocytes (Figures 5C–5E). Treatment with the γ-secretase inhibitor DAPT had no effect on the metabolism of the astrocytes (Figures 5C–5E). Since increased oxidative stress has been suggested to play a crucial role in AD pathology (Beal, 2005; Lovell and Markesbery, 2007), we measured cellular oxidative stress using CellROX, a fluorogenic probe, which becomes fluorescent upon oxidation. *PSEN1 ΔE9* astrocytes showed significantly increased levels of intracellular reactive oxygen species (ROS) when compared with isogenic control cells (Figures 5F and 5G). As the decreased glycolysis also suggested a reduction in lactate production, we further measured L(+)-lactate secretion. As expected, lactate secretion to the media was significantly higher from the control than from the *PSEN1 ΔE9* astrocytes (Figure 5H). These data show that *PSEN1 ΔE9* astrocytes are more oxidative than

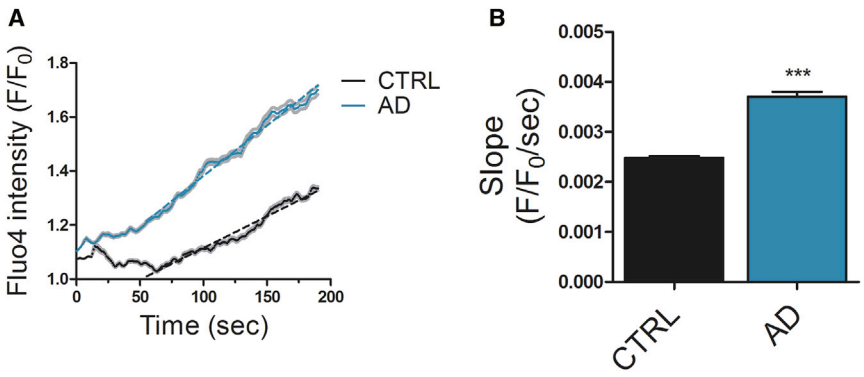

Figure 3. Ca^{2+} Homeostasis Is Disturbed in AD Astrocytes

(A) Dynamics of Ca^{2+} leakage from the ER in the presence of 50 μM ryanodine, 100 μM 2APB, and 1 μM thapsigargin. Solid lines represent average traces with SEM (in gray) and dotted lines the linear fit for slope measurement. Representative traces from one control and one AD line are shown.

(B) Quantification of the rate of Ca^{2+} leakage (slope) from the linear range of the traces. Data are presented as mean ± SEM from three independent experiments (CTRL, n = 814 cells; AD, n = 540 cells; ***p < 0.001).

See also Figure S5.

the glycolytic control astrocytes, generating more ROS and oxidative stress, and producing less lactate.

PSEN1 ΔE9 Mutant Astrocytes Alter the Calcium Signaling Activity of Healthy Neurons

Finally, we established a 3D co-culture model of neurons and astrocytes to study whether *PSEN1 ΔE9* mutant astrocytes have functional effects on neurons. We utilized a previously described (Choi et al., 2014) thin-layer Matrigel model to culture isogenic control neurons together with either isogenic control or *PSEN1 ΔE9* mutant astrocytes (Figure 6A). Application of glutamate, together with the co-agonist glycine, resulted in significantly lower Ca^{2+}-transient amplitudes in healthy control neurons co-cultured with AD astrocytes when compared with the same neurons co-cultured with control astrocytes (Figures 6B–6D). Likewise, the presence of AD astrocytes also significantly reduced the neuronal Ca^{2+} transients evoked by γ-aminobutyric acid (GABA) (Figures 6B, 6C, and 6E). These results show that the *PSEN1 ΔE9* astrocytes trigger functional consequences on healthy neurons.

DISCUSSION

Current knowledge of the mechanisms underlying AD pathology mostly arises from animal models, which do not truly recapitulate the human disease. Given the differences in complexity between human and rodent astrocytes (Oberheim et al., 2009), the contribution of astrocytes to disease progression is most likely under-represented in the animal models. By generating astrocytes from AD patients with mutant *PSEN1*, we show that the pathogenic *PSEN1 ΔE9* mutation leads to a severe phenotype in AD astrocytes, affecting Aβ production, cytokine secretion, Ca^{2+} homeostasis, mitochondrial metabolism, ROS production, and lactate secretion, and provides evidence of the importance of astrocytes in AD pathology.

One of the hallmarks of AD pathology is the accumulation of Aβ peptides in the patient's brain. Astrocytes are thought to play a critical role in Aβ clearance (Ries and Sastre, 2016), while neurons have generally been considered as the main Aβ producers (Zhao et al., 1996). However, astrocytes may also contribute to Aβ production (Liao et al., 2016; Zhao et al., 2011). Our iPSC-derived AD astrocytes both secrete increased levels of Aβ1–42 and show decreased uptake, suggesting that astrocytes contribute to the amyloid plaque formation in AD by both increased release and compromised clearance of Aβ1–42. *PSEN1* mutations have previously been reported to both activate and inactivate γ-secretase activity (Sun et al., 2017; Veugelen et al., 2016; Xia et al., 2015). In our iPSC-derived cells, *PSEN1 ΔE9* mutation had no effect on the overall enzymatic activity of γ-secretase and one copy of the *PSEN1 ΔE9* deletion significantly increased Aβ1–42 secretion in both astrocytes and neurons, while in a recent report the *PSEN1 ΔE9* point mutation was shown to increase Aβ1–40 production in AD neurons (Woodruff et al., 2013). Several factors may contribute to the discrepancies seen between different studies. Vast clinical heterogeneity is seen between different patients with the *PSEN1 ΔE9* mutation (Crook et al., 1998; Hiltunen et al., 2000), suggesting putative variability also in Aβ processing, which is likely to be context dependent and cell-type dependent. Furthermore, different studies have used different methods for assessing γ-secretase activity. We looked for general enzymatic activity while some studies have examined specific substrates such as N-cadherin (Woodruff et al., 2013), which may further complicate comparison of different studies. iPSC-derived cells may help determine the factors contributing to these controversies in γ-secretase activity and Aβ production among different studies.

Ca^{2+} homeostasis has been proposed to play a crucial role in AD disease progression (Berridge, 2011; Green and LaFerla, 2008). *PSEN1* is known to have a direct function in Ca^{2+} signaling, and mutations in *PSEN1* disturb ER Ca^{2+}

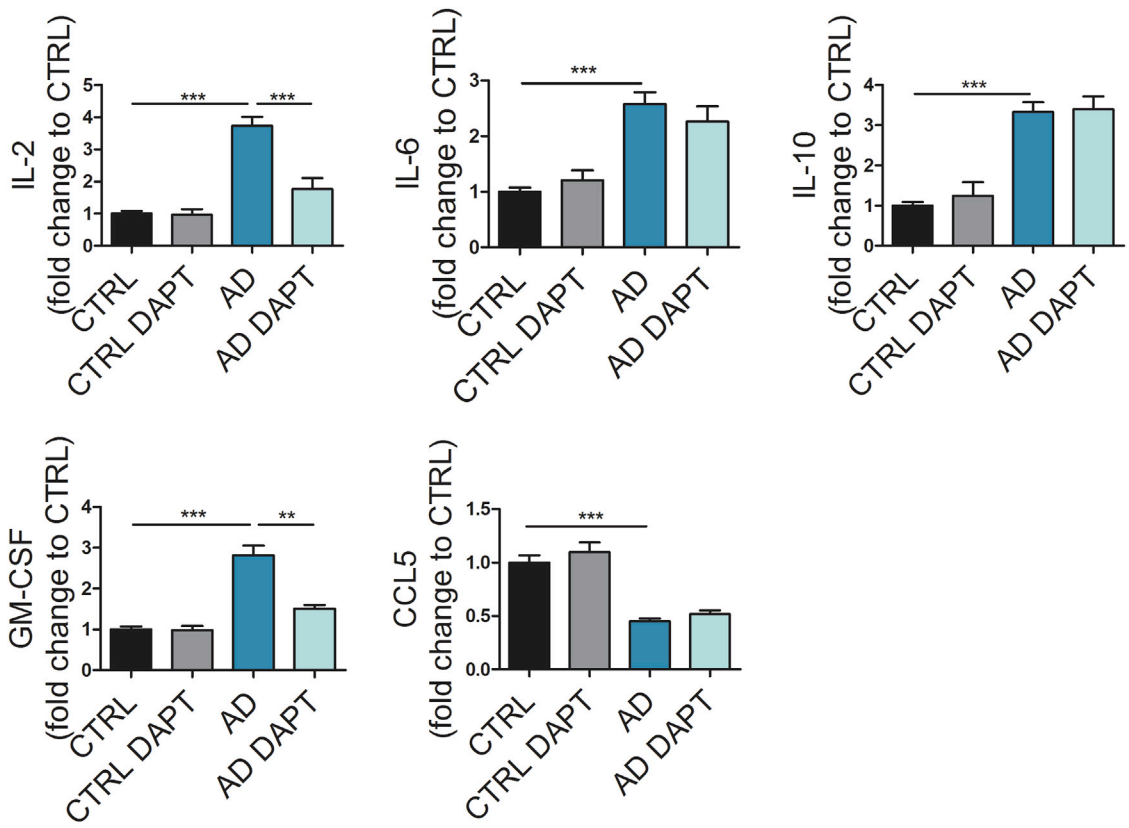

Figure 4. AD Astrocytes Show Altered Cytokine Release in Pro-inflammatory Conditions

Concentrations of IL-2, IL-6, IL-10, GM-CSF, and CCL5 were quantified from media after stimulation with TNFα (50 ng/mL) and IL-1β (10 ng/mL) for 48 hr with CBA assay. Results are shown as fold change to control lines. DAPT: cells were treated with γ-secretase inhibitor DAPT simultaneously with TNFα and IL-1β stimulation. Data are presented as mean ± SEM from three independent experiments (CTRL, n = 6 lines; AD, n = 6 lines; $^{**}p < 0.01$, $^{***}p < 0.001$). See also Figure S3.

pools (Bezprozvanny and Mattson, 2008; Ito et al., 1994). However, the mechanisms of how *PSEN1* mutations affect Ca^{2+} homeostasis are not clear. Increase in expression or activity of intracellular Ca^{2+} channels such as RyR or IP_3R has been proposed (Chan et al., 2000; Cheung et al., 2008), as well as activation of SERCA Ca^{2+} pumps (Green et al., 2008). Furthermore, presenilins themselves have been suggested to form passive Ca^{2+} leak channels in the ER (Kuo et al., 2015; Tu et al., 2006). In the present study, *PSEN1* mutant AD astrocytes showed increased passive Ca^{2+} leak from the ER, which could result from the accumulation of full-length PS-1 protein also shown in this study, and its putative ability to form Ca^{2+} leak channels in the ER.

Emerging evidence suggests that inflammation actively contributes to AD pathology (Zhang et al., 2013). Astrocytes are well known to respond to, produce, and secrete many cytokines, and they can contribute to both pro-inflammatory and anti-inflammatory signaling (Sofroniew, 2014). The release of cytokines is known to change during AD disease progression (Heneka et al., 2015), and cytokine levels in the cerebrospinal fluid have been considered as putative biomarkers for AD disease progression. Accordingly, we observed that inflammatory stimulation led to altered cytokine release from AD astrocytes when compared with control cells and, interestingly, γ-secretase inhibition was able to partially normalize this, suggesting that the inflammatory response is related to Aβ pathology. Thus, iPSC-derived cells may provide a new tool to identify early alterations in cytokine release that could be used as biomarkers for the disease.

Oxidative stress is considered an early event preceding Aβ deposits and has been proposed to play a crucial role in AD pathology (Nunomura et al., 2001; Pratico et al., 2001). Neurons are the highly respirative cells in the brain (Belanger et al., 2011), and mitochondrial respiration is a major producer of ROS. We show here that the *PSEN1 ΔE9* mutation switches the metabolism of AD astrocytes toward oxidative phosphorylation, whereas control cells are more glycolytic, as is typical for astrocytes (Belanger et al., 2011). Moreover, treatment with γ-secretase inhibitor did not attenuate the

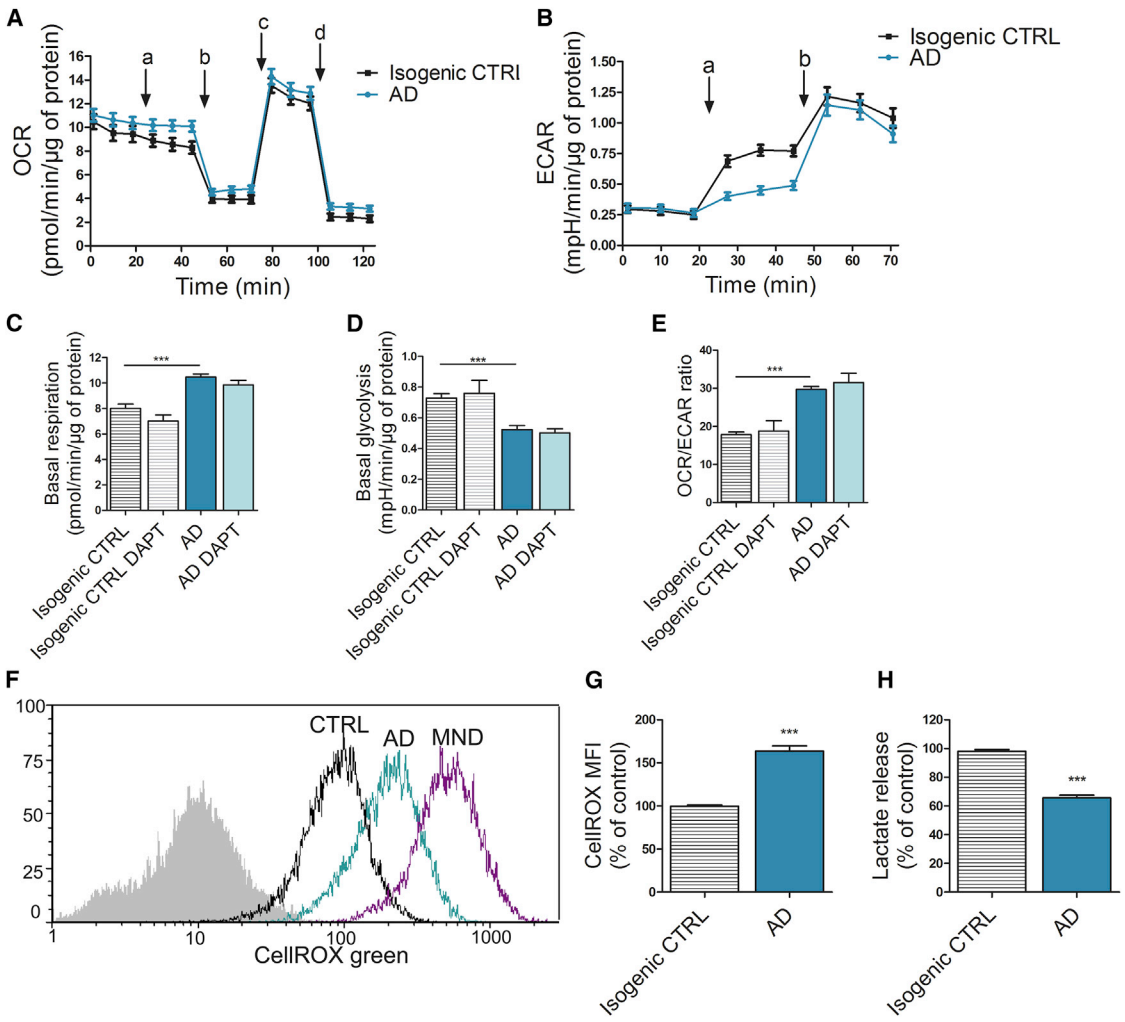

Figure 5. Altered Mitochondrial Metabolism in AD Astrocytes Leads to Increased ROS Production and Reduced Lactate Secretion

(A) Oxygen consumption rate (OCR) following sequential additions of 10 µM glucose (a), 1 µM oligomycin (b), 1 µM FCCP (c), and 1 µM antimycin A and rotenone (d). Results are normalized to protein content. Three independent experiments (n = 30 replicates/group from 2 isogenic pairs).

(B) Extracellular acidification rate following sequential additions of 10 µM glucose (a) and 1 µM oligomycin (b). Results are normalized to protein content. Three independent experiments (n = 30 replicates/group from 2 isogenic pairs).

(C–E) Basal respiration (C) and basal glycolysis (D) were quantified after glucose addition from OCR and ECAR curves, respectively. The OCR/ECAR ratio (E) was calculated after glucose addition to determine the metabolic profile of astrocytes. DAPT: cells were treated with γ-secretase inhibitor DAPT before experiments. ***$p < 0.001$.

(F) Representative median fluorescent intensity FACS histograms from CellROX analysis. Non-stained cells are shown in gray, isogenic control cells in black, and AD cells in turquoise. Menadione (MND)-treated cells (violet) were used as a positive control.

(G) Quantification of ROS production with CellROX green probe showing median fluorescent intensities (MFI) as a percentage of control group. Three independent experiments (n = 25–30 replicates/group from 2 isogenic pairs; ***$p < 0.001$).

(H) Lactate release was quantified from media with an enzymatic assay and normalized to protein content. Three independent experiments (n = 30 replicates/group from 2 isogenic pairs; ***$p < 0.001$).

All data are presented as mean ± SEM. See also Figure S1.

changes in mitochondrial metabolism, indicating that this phenotype could be independent of the Aβ pathology. The increase in respiratory function leads to increased ROS production by astrocytes, suggesting that astrocytes contribute to increased oxidative stress in AD brain. Furthermore, the concomitant decrease in glycolytic activity resulted in reduced lactate production, thus disturbing the astrocyte-neuron lactate shuttling and compromising energy supply

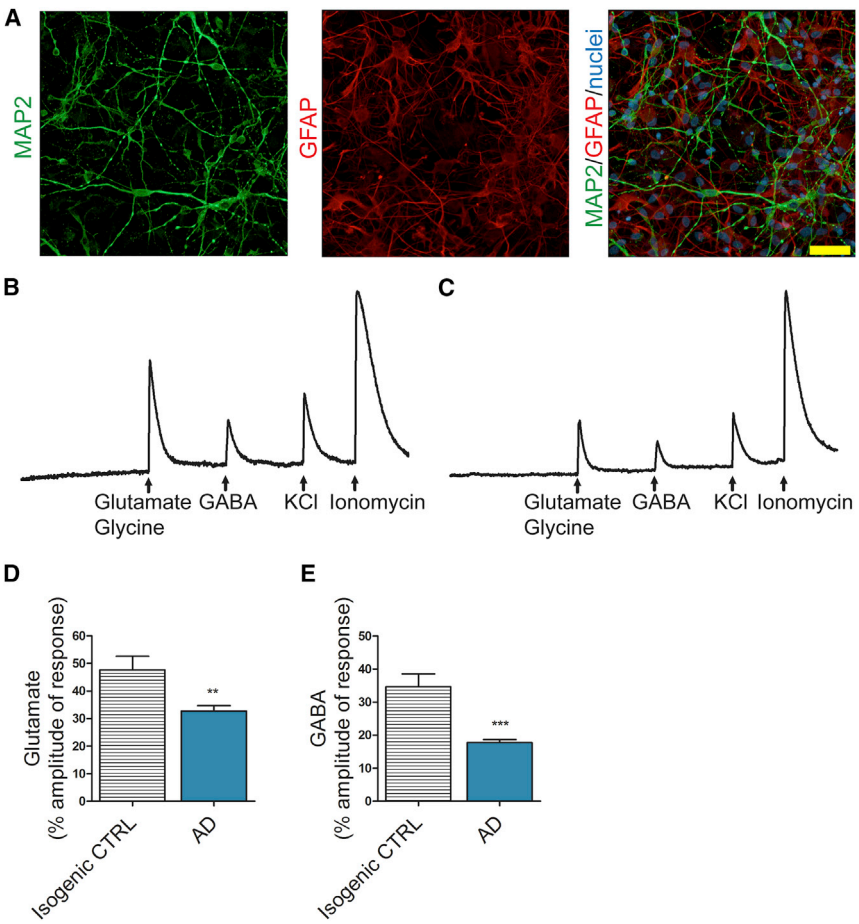

Figure 6. AD Astrocytes Influence the Calcium Signaling Activity of Healthy Neurons

(A) Representative immunocytochemistry image of the thin-layer Matrigel co-culture with MAP2-positive neurons (green) and GFAP-positive astrocytes (red). Nuclei are stained with Hoechst. Scale bar, 50 μm.

(B) Representative electrogram of isogenic control neurons co-cultured with isogenic control astrocytes showing Ca^{2+} amplitudes in response to applications of glutamate and glycine, GABA, KCl, and ionomycin.

(C) Representative electrogram of isogenic control neurons co-cultured with AD astrocytes showing Ca^{2+} amplitudes in response to applications of glutamate and glycine, GABA, KCl, and ionomycin.

(D) Quantification of the Ca^{2+} amplitudes in response to glutamate and glycine application. The x axis shows the genotype of the astrocytes (isogenic CTRL, n = 35 cells; AD, n = 134 cells from 3 independent experiments with 2 isogenic pairs; $^{**}p < 0.01$).

(E) Quantification of the Ca^{2+} amplitudes in response to GABA application. The x axis shows the genotype of the astrocytes (isogenic CTRL, n = 27 cells; AD, n = 132 cells from 3 independent experiments with 2 isogenic pairs; $^{***}p < 0.001$).

Data are presented as mean ± SEM. See also Figure S1.

to neurons (Figley, 2011; Pellerin and Magistretti, 1994). As rat studies have shown that lactate produced and released by astrocytes is essential for memory formation (Suzuki et al., 2011), the reduced lactate secretion by astrocytes might well contribute to dementia in AD.

The importance of astrocytes in neurodegenerative disorders such as AD is becoming more and more evident with accumulating data (Birch, 2014). Recent iPSC-based studies have shown aberrant morphological changes in AD astrocytes (Jones et al., 2017), as well as APOE-related neurotrophic disturbances (Zhao et al., 2017). In our study, AD astrocytes were able to alter Ca^{2+} signaling activity of healthy control neurons, further proving the importance of proper astrocyte-neuron interplay in AD.

Currently, there are no effective therapy options for AD. Most clinical trials have focused on either reducing the production or inducing the clearance of Aβ, but all have thus far failed (Castello et al., 2014; Golde et al., 2011). However, new approaches are tested constantly, and a recent trial with antibody-based immunotherapy against Aβ showed promise (Sevigny et al., 2016). Dysregulated Ca^{2+} homeostasis has also been proposed as a putative therapeutic target in AD (Briggs et al., 2017), and a few trials with dantrolene, an RyR inhibitor, have been promising. For example, a short-term treatment was shown to reduce neuropathology in AD mice (Peng et al., 2012). A third treatment strategy aims at reducing oxidative stress (Gella and Durany, 2009). Our AD astrocytes secrete considerable amounts of Aβ1–42, show altered Ca^{2+} homeostasis, and produce increased amounts of ROS, thus providing a unique tool for preclinical treatment trials with all these major approaches.

In conclusion, our data show that *PSEN1* mutant astrocytes manifest a severe disease phenotype and are likely to contribute significantly to AD progression. Furthermore, as the cells manifest hallmarks of the disease and the major targets for therapeutics, they provide an excellent platform for drug trials.

EXPERIMENTAL PROCEDURES

Generation of iPSCs

Dermal biopsies and blood samples were collected after informed consent and approval from the committee on Research Ethics of Northern Savo Hospital district (license no. 123/2016). Fibroblasts

and peripheral blood mononuclear cells T cells were isolated and cultured as previously described (Korhonen et al., 2015; Qu et al., 2013). Somatic cells were reprogrammed to iPSCs with either lentiviral vectors, CytoTune -iPS 1.0, or CytoTune -iPS 2.0 Sendai Reprogramming Kits (Invitrogen) as previously described (Holmqvist et al., 2016). iPSCs were grown on Matrigel-coated (Corning) plates in Essential 8 Medium (E8; Life Technologies) and passaged with 0.5 mM EDTA in the presence of 5 μM Y-27632 ROCK inhibitor (Selleckchem). Isogenic control lines were generated according to a previously published protocol (Chen et al., 2015). Further details are provided in Supplemental Experimental Procedures.

Astroglial Differentiation of iPSCs

The astroglial differentiation protocol was modified from previously described protocols (Chambers et al., 2009; Krencik et al., 2011). Differentiation was started by changing to neural differentiation medium (NDM) consisting of DMEM/F12 and Neurobasal (1:1), 1% B27 without vitamin A, 0.5% N2, 1% Glutamax, and 0.5% penicillin/streptomycin (50 IU/50 μg/mL) (all from Invitrogen) supplemented with dual SMAD inhibitors 10 μM SB431542 (Sigma) and 200 nM LDN193189 (Selleckchem). Medium was changed daily for 12 days or until rosette-like structures started to emerge. Cells were then cultured in NDM supplemented with 20 ng/mL basic fibroblast growth factor (bFGF) for 2–3 days to expand the rosettes. Areas with rosettes were mechanically lifted and cultured in suspension on ultra-low attachment plates (Corning) in NDM for 2 days to allow sphere formation. Neural progenitor spheres were maintained in astrocyte differentiation medium (ADM) consisting of DMEM/F12, 1% N2, 1% Glutamax, 1% non-essential amino acids, 0.5% penicillin/streptomycin (50 IU/50 μg/mL), and 0.5 IU/mL heparin (Leo Pharma) supplemented with 10 ng/mL bFGF and 10 ng/mL EGF (Peprotech). Medium was changed every 2–3 days and spheres were split manually every week. Spheres were maintained in suspension for 5–7 months to ensure pure astroglial cultures. For maturation, spheres were dissociated with Accutase (STEMCELL Technologies) and plated on Matrigel-coated dishes in ADM supplemented with 10 ng/mL CNTF and 10 ng/mL BMP4 (both from Peprotech) 7 days prior to experiments.

Glucose Uptake Assay

Glucose uptake was determined as previously published (Yamamoto et al., 2015) with slight modifications. In brief, cells were loaded with glucose-free medium in the absence or presence of 120 μM 2-[N-(7-nitrobenz-2-oxa-1,3-diazol-4-yl) amino]-2-deoxy-D-glucose (2-NBDG, Thermo Fisher) for 30 min in 5% CO_2 at 37°C. The 2-NBDG uptake was stopped by washing the cells twice with PBS. Cells were detached with Accutase and resuspended in PBS prior to flow-cytometric measurement. Data from 15,000 single live cell events were collected using FACSCalibur (BD Biosciences, San Jose, CA, USA).

Glutathione Secretion Assay

Glutathione measurements were performed as described earlier (Liddell et al., 2006) by mixing the medium with an equal volume of cold sulfosalicylic acid (1% in water). Samples were further diluted 1:5 with water before the measurements. Glutathione concentrations were determined from standard curve and normalized to total protein amount using a Pierce BCA protein assay according to the manufacturer's instructions (Thermo Fisher).

Aβ and γ-Secretase Assays

Aβ1–40 and Aβ1–42 amounts were measured from the culture medium conditioned for 72 hr with ELISA according to the manufacturer's instructions (Invitrogen). DAPT (5 μM; Sigma) was added to the medium 1 day prior to the conditioning when applicable. Results were normalized to total protein concentration (Pierce BCA protein assay). Fluorochrome-conjugated Aβ1–42 (HiLyte Fluor 488-labeled, AnaSpec) was mixed with non-fluorescent fibrilized Aβ1–42 (from American Peptides, incubated at +37°C for 1 week) in a 1:15 ratio and added to the cells at a final concentration of 5 μM. Cells were incubated overnight, washed three times with PBS to remove non-internalized Aβ, and detached with Accutase. The percentage of 488-positive cells was determined with FACSCalibur (BD Biosciences). γ-Secretase activity was measured following a previously published protocol (Farmery et al., 2003; Viswanathan et al., 2011). γ-Secretase inhibitor L685,458 (Sigma) was included for assay validation purposes.

Ca^{2+} Imaging

Ca^{2+} signals from astrocytes were recorded with a confocal microscope, and data were analyzed as previously described (Mutikainen et al., 2016). All experiments were carried out at 37°C. Cells were loaded with Fluo4 (Fluo-4-acetoxymethyl [AM]-ester, Life Technologies; 5 μM for 20 min), rinsed with Hank's balanced salt solution (HBSS) containing 2 mM $CaCl_2$, and transferred to the recording chamber (Cell MicroControls; flow rate approximately 1–2 mL/min, chamber volume 0.4 mL). Ca-free 1 mM EGTA-containing HBSS was applied for 3 min for baseline recordings. For the estimation of non-specific Ca^{2+} leak from the ER, 1 μM thapsigargin, 50 μM ryanodine, and 100 μM 2APB were applied. All compounds were diluted in Ca^{2+}-free HBSS with 1 mM EGTA. To investigate intercellular propagation of Ca^{2+} waves, we used local electrical stimulation. A glass patch pipette (~1 MΩ) filled with bath solution was placed close to an astrocyte. A platinum stimulating electrode was placed into the pipette and an additional two ground platinum electrodes were placed in the bath area at both sides of the cell. Two-second square stimulation trains at 20-Hz frequency with pulse duration of 2 ms were used.

For co-culture experiments, cells were first loaded with Fluo4, followed by a 10-min washout with a basic solution containing 152 mM NaCl, 10 mM glucose, 10 mM HEPES, 2.5 mM KCl, 2 mM $CaCl_2$, and 1 mM $MgCl_2$ (pH 7.4). Cells were then transferred to the recording chamber continuously rinsed with the same basic solution. Fluorescent signals were acquired with an Olympus IX70 microscope on the Till Photonics imaging setup (FEI) equipped with a 12-bit CCD Camera (SensiCam) with a light excitation wavelength of 494 nm and adequate filters. Glutamate (100 μM; with the co-agonist glycine 10 μM) or GABA (100 μM) were applied for 2 s by a fast perfusion system (RSC-200). Depolarizing solution containing 30 mM KCl was then applied to distinguish neurons from other cell types. At the end, cells were challenged with ionomycin (10 μM, 2 s) for normalization of the tested signals.

Cytometric Bead Array

A bead-based multiplex assay was used to analyze the cytokine secretion. Cytokine concentrations were detected by the cytometric bead array (CBA) Flex Sets (BD Biosciences) Human Soluble Protein (CCL5/RANTES, GM-CSF, and IL-6) and Human Enhanced Sensitivity (IL-2 and IL-10). The assay was done according to the manufacturer's instructions with minor modifications. For Soluble Protein, 20 μL of sample or cytokine standard and 20 μL of 1:50 bead mixture was used and for Enhanced Sensitivity, 25 μL of sample or cytokine standard and 10 μL of 1:20 bead mixture was used. Beads were acquired on FACSAriaIII (BD Biosciences). At least 300 events per cytokine were measured. Data were analyzed using FCAP Array 2.0 (SoftFlow, Hungary) and cytokine concentrations were calculated by regression analysis from known standard concentrations.

Cellular Metabolism, ROS, and Lactate Analysis

Cellular metabolism was analyzed with the Seahorse XF24 analyzer and Mito Stress Test according to the manufacturer's instructions (Agilent Technologies). Assay medium was supplemented with 1× Glutamax and 0.5 mM sodium pyruvate. Glucose (10 mM) was added during the assay. Final concentrations of oligomycin, FCCP (carbonyl cyanide-4-phenylhydrazone), antimycin, and rotenone were 1 μM each. Results were normalized to total protein content (Pierce BCA protein assay). For ROS measurement, cells were loaded with 1 μM CellROX green reagent (Molecular Probes) for 45 min. Menadione (50 μM; Sigma) was used as a positive control and added together with CellROX. Median fluorescent intensities (MFI) of 10,000 single cell events from each sample were collected using FACSCalibur (BD Biosciences). L(+)-lactate was measured from the conditioned medium (24 hr) using a colorimetric Lactate Assay kit (Sigma) according to the manufacturer's instructions. Results were normalized to total protein amount (Pierce BCA protein assay).

3D Co-cultures

Thin-layer Matrigel co-cultures were prepared as described in Choi et al. (2014) with slight modifications. In brief, equal amounts of iPSC-derived astrocytes and neurons were mixed and resuspended with 1:10 diluted Matrigel to a final concentration of 1×10^6 cells/mL. Cell suspension was plated on poly-L-ornithine-coated coverslips and left to polymerize overnight. Wells were filled with NDM medium on the next day and the medium was changed twice a week. Cells were kept in co-cultures for 4–6 weeks before experiments.

Statistical Analyses

Statistical analyses were performed with GraphPad Prism 5.03 software (GraphPad Software) using Student's t test or one-way ANOVA with Tukey's post hoc test. For calcium imaging, data were analyzed with Origin9 software (OriginLab, Northampton, MA, USA) using one-way ANOVA with Fisher's post hoc test or Student's t test. Statistical significance was assumed at $p < 0.05$. All data are expressed as mean ± SEM.

SUPPLEMENTAL INFORMATION

Supplemental Information includes Supplemental Experimental Procedures, five figures, and one table and can be found with this article online at https://doi.org/10.1016/j.stemcr.2017.10.016.

AUTHOR CONTRIBUTIONS

M.O. performed most experiments and analyzed data. K.P. and Š.L. contributed to the generation and characterization of iPSCs and astrocytes. A.J.P. and S.-C.Z. designed the isogenic controls, constructed and provided plasmids, and advised on astrocyte differentiation. N.N., A.S., and P.T. performed and analyzed Ca^{2+} imaging of astrocytes. M.G.O. and R.G. performed and analyzed Ca^{2+} imaging of co-cultures. M.V. and J.O.R. provided patient cells. S.L., T.S., M.H., and A.H. performed and analyzed western blots and GS activity and provided GS inhibitors. M.O., K.M.K., R.H.H., and J.K. conceived and designed the study. M.O., R.H.H., and J.K. interpreted the data and wrote the manuscript.

ACKNOWLEDGMENTS

We thank L. Kaskela, E. Korhonen, M. Tikkanen, S. Wojciechowski, S. Lemarchant, and I. Hyötyläinen for technical assistance and M. Ruponen, J. Jones, R. Bradley, and J. Knackert for advice in iPSC and astrocyte cultures. This work was supported by the University of Eastern Finland, the Academy of Finland, European Union's Horizon 2020 Research and Innovation Program (grant agreement no. 643417), Sigrid Jusélius Foundation, the Finnish Funding Agency for Innovation (Tekes), the Emil Aaltonen Foundation, the Northern Savo Cultural Foundation, and Fulbright Center Finland. S.-C.Z. is co-founder of BrainXell. J.K. is a co-owner of Aranda Pharma and a consultant of Orthogonal Neuroscience. J.O.R. serves as a neurology consultant for Clinical Research Services Turku (CRST).

Received: June 11, 2017
Revised: October 19, 2017
Accepted: October 19, 2017
Published: November 16, 2017

REFERENCES

Beal, M.F. (2005). Oxidative damage as an early marker of Alzheimer's disease and mild cognitive impairment. Neurobiol. Aging *26*, 585–586.

Belanger, M., Allaman, I., and Magistretti, P.J. (2011). Brain energy metabolism: focus on astrocyte-neuron metabolic cooperation. Cell Metab *14*, 724–738.

Berridge, M.J. (2011). Calcium signalling and Alzheimer's disease. Neurochem. Res. *36*, 1149–1156.

Bezprozvanny, I., and Mattson, M.P. (2008). Neuronal calcium mishandling and the pathogenesis of Alzheimer's disease. Trends Neurosci. *31*, 454–463.

Birch, A.M. (2014). The contribution of astrocytes to Alzheimer's disease. Biochem. Soc. Trans. *42*, 1316–1320.

Blennow, K., de Leon, M.J., and Zetterberg, H. (2006). Alzheimer's disease. Lancet *368*, 387–403.

Briggs, C.A., Chakroborty, S., and Stutzmann, G.E. (2017). Emerging pathways driving early synaptic pathology in Alzheimer's disease. Biochem. Biophys. Res. Commun. *483*, 988–997.

Castello, M.A., Jeppson, J.D., and Soriano, S. (2014). Moving beyond anti-amyloid therapy for the prevention and treatment of Alzheimer's disease. BMC Neurol. *14*, 169.

Cedazo-Minguez, A., Popescu, B.O., Ankarcrona, M., Nishimura, T., and Cowburn, R.F. (2002). The presenilin 1 deltaE9 mutation gives enhanced basal phospholipase C activity and a resultant increase in intracellular calcium concentrations. J. Biol. Chem. *277*, 36646–36655.

Chambers, S.M., Fasano, C.A., Papapetrou, E.P., Tomishima, M., Sadelain, M., and Studer, L. (2009). Highly efficient neural conversion of human ES and iPS cells by dual inhibition of SMAD signaling. Nat. Biotechnol. *27*, 275–280.

Chan, S.L., Mayne, M., Holden, C.P., Geiger, J.D., and Mattson, M.P. (2000). Presenilin-1 mutations increase levels of ryanodine receptors and calcium release in PC12 cells and cortical neurons. J. Biol. Chem. *275*, 18195–18200.

Chen, Y., Cao, J., Xiong, M., Petersen, A.J., Dong, Y., Tao, Y., Huang, C.T., Du, Z., and Zhang, S.C. (2015). Engineering human stem cell lines with inducible gene knockout using CRISPR/Cas9. Cell Stem Cell *17*, 233–244.

Cheung, K.H., Shineman, D., Muller, M., Cardenas, C., Mei, L., Yang, J., Tomita, T., Iwatsubo, T., Lee, V.M., and Foskett, J.K. (2008). Mechanism of Ca^{2+} disruption in Alzheimer's disease by presenilin regulation of InsP3 receptor channel gating. Neuron *58*, 871–883.

Choi, S.H., Kim, Y.H., Hebisch, M., Sliwinski, C., Lee, S., D'Avanzo, C., Chen, H., Hooli, B., Asselin, C., Muffat, J., et al. (2014). A three-dimensional human neural cell culture model of Alzheimer's disease. Nature *515*, 274–278.

Crook, R., Verkkoniemi, A., Perez-Tur, J., Mehta, N., Baker, M., Houlden, H., Farrer, M., Hutton, M., Lincoln, S., Hardy, J., et al. (1998). A variant of Alzheimer's disease with spastic paraparesis and unusual plaques due to deletion of exon 9 of presenilin 1. Nat. Med. *4*, 452–455.

Farmery, M.R., Tjernberg, L.O., Pursglove, S.E., Bergman, A., Winblad, B., and Naslund, J. (2003). Partial purification and characterization of gamma-secretase from post-mortem human brain. J. Biol. Chem. *278*, 24277–24284.

Figley, C.R. (2011). Lactate transport and metabolism in the human brain: implications for the astrocyte-neuron lactate shuttle hypothesis. J. Neurosci. *31*, 4768–4770.

Gella, A., and Durany, N. (2009). Oxidative stress in Alzheimer disease. Cell Adh Migr *3*, 88–93.

Golde, T.E., Schneider, L.S., and Koo, E.H. (2011). Anti-Aβ therapeutics in Alzheimer's disease: the need for a paradigm shift. Neuron *69*, 203–213.

Green, K.N., Demuro, A., Akbari, Y., Hitt, B.D., Smith, I.F., Parker, I., and LaFerla, F.M. (2008). SERCA pump activity is physiologically regulated by presenilin and regulates amyloid β production. J. Cell Biol *181*, 1107–1116.

Green, K.N., and LaFerla, F.M. (2008). Linking calcium to Abeta and Alzheimer's disease. Neuron *59*, 190–194.

Hardy, J., and Selkoe, D.J. (2002). The amyloid hypothesis of Alzheimer's disease: progress and problems on the road to therapeutics. Science *297*, 353–356.

Heneka, M.T., Carson, M.J., El Khoury, J., Landreth, G.E., Brosseron, F., Feinstein, D.L., Jacobs, A.H., Wyss-Coray, T., Vitorica, J., Ransohoff, R.M., et al. (2015). Neuroinflammation in Alzheimer's disease. Lancet Neurol. *14*, 388–405.

Hiltunen, M., Helisalmi, S., Mannermaa, A., Alafuzoff, I., Koivisto, A.M., Lehtovirta, M., Pirskanen, M., Sulkava, R., Verkkoniemi, A., and Soininen, H. (2000). Identification of a novel 4.6-kb genomic deletion in presenilin-1 gene which results in exclusion of exon 9 in a Finnish early onset Alzheimer's disease family: an Alu core sequence-stimulated recombination? Eur. J. Hum. Genet. *8*, 259–266.

Holmqvist, S., Lehtonen, S., Chumarina, M., Puttonen, K.A., Azevedo, C., Lebedeva, O., Ruponen, M., Oksanen, M., Djellou, M., Collin, A., et al. (2016). Creation of a library of induced pluripotent stem cells from Parkinsonian patients. NPJ Parkinsons Dis. *2*, 16009.

Ito, E., Oka, K., Etcheberrigaray, R., Nelson, T.J., McPhie, D.L., Tofel-Grehl, B., Gibson, G.E., and Alkon, D.L. (1994). Internal Ca^{2+} mobilization is altered in fibroblasts from patients with Alzheimer disease. Proc. Natl. Acad. Sci. USA *91*, 534–538.

Jones, V.C., Atkinson-Dell, R., Verkhratsky, A., and Mohamet, L. (2017). Aberrant iPSC-derived human astrocytes in Alzheimer's disease. Cell Death Dis *8*, e2696.

Kondo, T., Asai, M., Tsukita, K., Kutoku, Y., Ohsawa, Y., Sunada, Y., Imamura, K., Egawa, N., Yahata, N., Okita, K., et al. (2013). Modeling Alzheimer's disease with iPSCs reveals stress phenotypes associated with intracellular Aβ and differential drug responsiveness. Cell Stem Cell *12*, 487–496.

Korhonen, P., Kanninen, K.M., Lehtonen, S., Lemarchant, S., Puttonen, K.A., Oksanen, M., Dhungana, H., Loppi, S., Pollari, E., Wojciechowski, S., et al. (2015). Immunomodulation by interleukin-33 is protective in stroke through modulation of inflammation. Brain Behav. Immun. *49*, 322–336.

Krencik, R., Weick, J.P., Liu, Y., Zhang, Z.J., and Zhang, S.C. (2011). Specification of transplantable astroglial subtypes from human pluripotent stem cells. Nat. Biotechnol. *29*, 528–534.

Kuo, I.Y., Hu, J., Ha, Y., and Ehrlich, B.E. (2015). Presenilin-like GxGD membrane proteases have dual roles as proteolytic enzymes and ion channels. J. Biol. Chem. *290*, 6419–6427.

Liao, M.C., Muratore, C.R., Gierahn, T.M., Sullivan, S.E., Srikanth, P., De Jager, P.L., Love, J.C., and Young-Pearse, T.L. (2016). Single-cell detection of secreted Aβ and sAPPα from human IPSC-derived neurons and astrocytes. J. Neurosci. *36*, 1730–1746.

Liddell, J.R., Hoepken, H.H., Crack, P.J., Robinson, S.R., and Dringen, R. (2006). Glutathione peroxidase 1 and glutathione are required to protect mouse astrocytes from iron-mediated hydrogen peroxide toxicity. J. Neurosci. Res. *84*, 578–586.

Lovell, M.A., and Markesbery, W.R. (2007). Oxidative damage in mild cognitive impairment and early Alzheimer's disease. J. Neurosci. Res. *85*, 3036–3040.

Magistri, M., Khoury, N., Mazza, E.M., Velmeshev, D., Lee, J.K., Bicciato, S., Tsoulfas, P., and Faghihi, M.A. (2016). A comparative transcriptomic analysis of astrocytes differentiation from human neural progenitor cells. Eur. J. Neurosci. *44*, 2858–2870.

Mutikainen, M., Tuomainen, T., Naumenko, N., Huusko, J., Smirin, B., Laidinen, S., Kokki, K., Hynynen, H., Yla-Herttuala, S.,

Heinaniemi, M., et al. (2016). Peroxisome proliferator-activated receptor-γ coactivator 1 α1 induces a cardiac excitation-contraction coupling phenotype without metabolic remodelling. J. Physiol. *594*, 7049–7071.

Nieweg, K., Andreyeva, A., van Stegen, B., Tanriover, G., and Gottmann, K. (2015). Alzheimer's disease-related amyloid-β induces synaptotoxicity in human iPS cell-derived neurons. Cell Death Dis *6*, e1709.

Nunomura, A., Perry, G., Aliev, G., Hirai, K., Takeda, A., Balraj, E.K., Jones, P.K., Ghanbari, H., Wataya, T., Shimohama, S., et al. (2001). Oxidative damage is the earliest event in Alzheimer disease. J. Neuropathol. Exp. Neurol. *60*, 759–767.

Oberheim, N.A., Takano, T., Han, X., He, W., Lin, J.H., Wang, F., Xu, Q., Wyatt, J.D., Pilcher, W., Ojemann, J.G., et al. (2009). Uniquely hominid features of adult human astrocytes. J. Neurosci. *29*, 3276–3287.

Oberheim, N.A., Wang, X., Goldman, S., and Nedergaard, M. (2006). Astrocytic complexity distinguishes the human brain. Trends Neurosci. *29*, 547–553.

Pellerin, L., and Magistretti, P.J. (1994). Glutamate uptake into astrocytes stimulates aerobic glycolysis: a mechanism coupling neuronal activity to glucose utilization. Proc. Natl. Acad. Sci. USA *91*, 10625–10629.

Peng, J., Liang, G., Inan, S., Wu, Z., Joseph, D.J., Meng, Q., Peng, Y., Eckenhoff, M.F., and Wei, H. (2012). Dantrolene ameliorates cognitive decline and neuropathology in Alzheimer triple transgenic mice. Neurosci. Lett. *516*, 274–279.

Pratico, D., Uryu, K., Leight, S., Trojanoswki, J.Q., and Lee, V.M. (2001). Increased lipid peroxidation precedes amyloid plaque formation in an animal model of Alzheimer amyloidosis. J. Neurosci. *21*, 4183–4187.

Qu, C., Puttonen, K.A., Lindeberg, H., Ruponen, M., Hovatta, O., Koistinaho, J., and Lammi, M.J. (2013). Chondrogenic differentiation of human pluripotent stem cells in chondrocyte co-culture. Int. J. Biochem. Cell Biol *45*, 1802–1812.

Ries, M., and Sastre, M. (2016). Mechanisms of Aβ clearance and degradation by glial cells. Front. Aging Neurosci. *8*, 160.

Sevigny, J., Chiao, P., Bussiere, T., Weinreb, P.H., Williams, L., Maier, M., Dunstan, R., Salloway, S., Chen, T., Ling, Y., et al. (2016). The antibody aducanumab reduces Aβ plaques in Alzheimer's disease. Nature *537*, 50–56.

Sofroniew, M.V. (2014). Multiple roles for astrocytes as effectors of cytokines and inflammatory mediators. Neuroscientist *20*, 160–172.

Sun, L., Zhou, R., Yang, G., and Shi, Y. (2017). Analysis of 138 pathogenic mutations in presenilin-1 on the in vitro production of Aβ42 and Aβ40 peptides by γ-secretase. Proc. Natl. Acad. Sci. USA *114*, E476–E485.

Suzuki, A., Stern, S.A., Bozdagi, O., Huntley, G.W., Walker, R.H., Magistretti, P.J., and Alberini, C.M. (2011). Astrocyte-neuron lactate transport is required for long-term memory formation. Cell *144*, 810–823.

Tarassishin, L., Suh, H.S., and Lee, S.C. (2014). LPS and IL-1 differentially activate mouse and human astrocytes: role of CD14. Glia *62*, 999–1013.

Thinakaran, G., Borchelt, D.R., Lee, M.K., Slunt, H.H., Spitzer, L., Kim, G., Ratovitsky, T., Davenport, F., Nordstedt, C., Seeger, M., et al. (1996). Endoproteolysis of presenilin 1 and accumulation of processed derivatives in vivo. Neuron *17*, 181–190.

Tu, H., Nelson, O., Bezprozvanny, A., Wang, Z., Lee, S.F., Hao, Y.H., Serneels, L., De Strooper, B., Yu, G., and Bezprozvanny, I. (2006). Presenilins form ER Ca^{2+} leak channels, a function disrupted by familial Alzheimer's disease-linked mutations. Cell *126*, 981–993.

Veugelen, S., Saito, T., Saido, T.C., Chavez-Gutierrez, L., and De Strooper, B. (2016). Familial Alzheimer's disease mutations in presenilin generate amyloidogenic Aβ peptide seeds. Neuron *90*, 410–416.

Vincent, A.J., Gasperini, R., Foa, L., and Small, D.H. (2010). Astrocytes in Alzheimer's disease: emerging roles in calcium dysregulation and synaptic plasticity. J. Alzheimers Dis. *22*, 699–714.

Viswanathan, J., Haapasalo, A., Bottcher, C., Miettinen, R., Kurkinen, K.M., Lu, A., Thomas, A., Maynard, C.J., Romano, D., Hyman, B.T., et al. (2011). Alzheimer's disease-associated ubiquilin-1 regulates presenilin-1 accumulation and aggresome formation. Traffic *12*, 330–348.

Waring, S.C., and Rosenberg, R.N. (2008). Genome-wide association studies in Alzheimer disease. Arch. Neurol. *65*, 329–334.

Woodruff, G., Young, J.E., Martinez, F.J., Buen, F., Gore, A., Kinaga, J., Li, Z., Yuan, S.H., Zhang, K., and Goldstein, L.S. (2013). The presenilin-1 ΔE9 mutation results in reduced gamma-secretase activity, but not total loss of PS1 function, in isogenic human stem cells. Cell Rep *5*, 974–985.

Xia, D., Watanabe, H., Wu, B., Lee, S.H., Li, Y., Tsvetkov, E., Bolshakov, V.Y., Shen, J., and Kelleher, R.J., 3rd. (2015). Presenilin-1 knockin mice reveal loss-of-function mechanism for familial Alzheimer's disease. Neuron *85*, 967–981.

Yamamoto, N., Ueda-Wakagi, M., Sato, T., Kawasaki, K., Sawada, K., Kawabata, K., Akagawa, M., and Ashida, H. (2015). Measurement of glucose uptake in cultured cells. Curr Protoc Pharmacol *71*, 12.14.1-12.14.26.

Zhang, B., Gaiteri, C., Bodea, L.G., Wang, Z., McElwee, J., Podtelezhnikov, A.A., Zhang, C., Xie, T., Tran, L., Dobrin, R., et al. (2013). Integrated systems approach identifies genetic nodes and networks in late-onset Alzheimer's disease. Cell *153*, 707–720.

Zhang, Y., Sloan, S.A., Clarke, L.E., Caneda, C., Plaza, C.A., Blumenthal, P.D., Vogel, H., Steinberg, G.K., Edwards, M.S., Li, G., et al. (2016). Purification and characterization of progenitor and mature human astrocytes reveals transcriptional and functional differences with mouse. Neuron *89*, 37–53.

Zhao, J., Davis, M.D., Martens, Y.A., Shinohara, M., Graff-Radford, N.R., Younkin, S.G., Wszolek, Z.K., Kanekiyo, T., and Bu, G. (2017). APOE ε4/ε4 diminishes neurotrophic function of human iPSC-derived astrocytes. Hum. Mol. Genet. *26*, 2690–2700.

Zhao, J., O'Connor, T., and Vassar, R. (2011). The contribution of activated astrocytes to Aβ production: implications for Alzheimer's disease pathogenesis. J. Neuroinflammation *8*, 150.

Zhao, J., Paganini, L., Mucke, L., Gordon, M., Refolo, L., Carman, M., Sinha, S., Oltersdorf, T., Lieberburg, I., and McConlogue, L. (1996). Beta-secretase processing of the beta-amyloid precursor protein in transgenic mice is efficient in neurons but inefficient in astrocytes. J. Biol. Chem. *271*, 31407–31411.

Stem Cell Reports, Volume *9*

Supplemental Information

PSEN1 Mutant iPSC-Derived Model Reveals Severe Astrocyte Pathology in Alzheimer's Disease

Minna Oksanen, Andrew J. Petersen, Nikolay Naumenko, Katja Puttonen, Šárka Lehtonen, Max Gubert Olivé, Anastasia Shakirzyanova, Stina Leskelä, Timo Sarajärvi, Matti Viitanen, Juha O. Rinne, Mikko Hiltunen, Annakaisa Haapasalo, Rashid Giniatullin, Pasi Tavi, Su-Chun Zhang, Katja M. Kanninen, Riikka H. Hämäläinen, and Jari Koistinaho

Figure S1

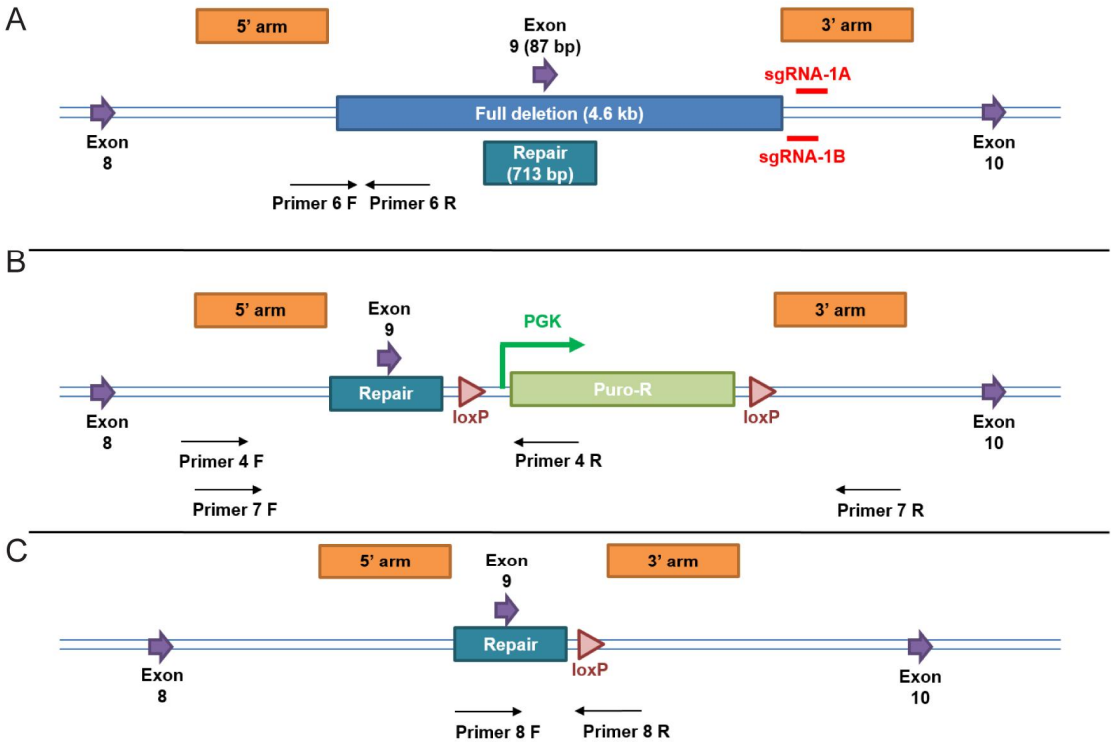
A
5' arm
Exon
9 (87 bp)
3' arm
sgRNA-1A
Full deletion (4.6 kb)
Exon
8
Repair
(713 bp)
sgRNA-1B
Exon
10
Primer 6 F
Primer 6 R
B
5' arm
Exon
9
PGK
3' arm
Repair
Puro-R
Exon
8
loxP
loxP
Exon
10
Primer 4 F
Primer 4 R
Primer 7 F
Primer 7 R
C
5' arm
Exon
9
3' arm
Repair
Exon
8
loxP
Exon
10
Primer 8 F
Primer 8 R

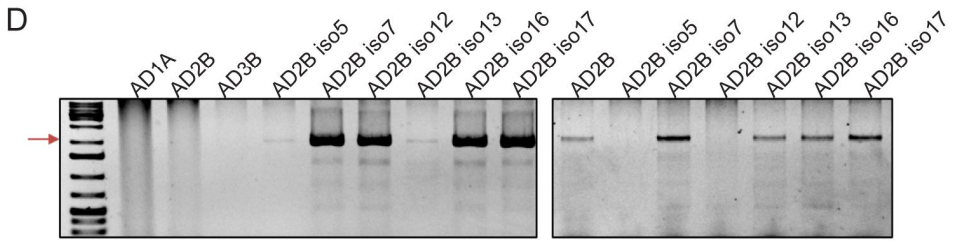
D
AD1A
AD2B
AD3B
AD2B iso5
AD2B iso7
AD2B iso12
AD2B iso13
AD2B iso16
AD2B iso17
AD2B
AD2B iso5
AD2B iso7
AD2B iso12
AD2B iso13
AD2B iso16
AD2B iso17

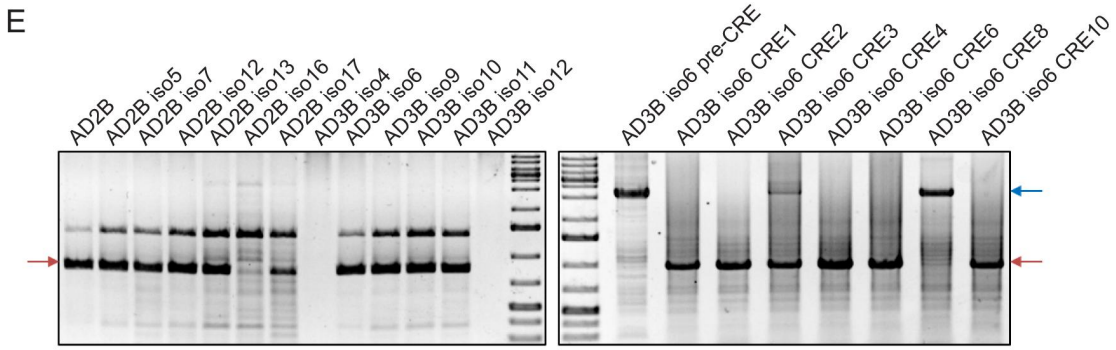
E
AD2B
AD2B iso5
AD2B iso7
AD2B iso12
AD2B iso13
AD2B iso16
AD2B iso17
AD3B iso4
AD3B iso6
AD3B iso9
AD3B iso10
AD3B iso11
AD3B iso12
AD3B iso6 pre-CRE
AD3B iso6 CRE1
AD3B iso6 CRE2
AD3B iso6 CRE3
AD3B iso6 CRE4
AD3B iso6 CRE6
AD3B iso6 CRE8
AD3B iso6 CRE10

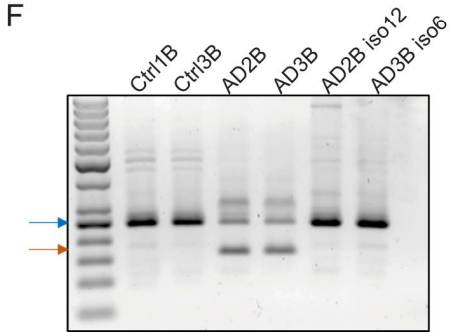
F
Ctrl1B
Ctrl3B
AD2B
AD3B
AD2B iso12
AD3B iso6

Figure S1. Schematic illustration of the generation of isogenic control lines. Related to Table 1 and Figures 1, 2, 5 and 6.

(A) The targeting strategy to correct the deletion of exon 9 in *PSEN1*. SgRNA pair was designed to target the + and – strands of DNA at the boundary of the full 4.6-kb full deletion. A homologous repair donor plasmid with 1 kb homology arms was designed to restore approximately 700 bp fragment containing exon 9 and the immediately-flanking intronic sequences, deemed sufficient for proper mRNA splicing without restoring the full-length intronic sequence.

(B) The targeted genomic region after successful electroporation. A LoxP-flanked PGK-puromycin cassette facilitates the selection of cells exhibiting homology directed repair at the *PSEN1* locus. PGK, phosphoglycerate kinase promoter; Puro-R, puromycin-resistance gene.

(C) The targeted genomic region after puromycin selection and CRE-recombinase treatment. To ensure proper *PSEN1* expression, the PGK-puromycin cassette was removed using CRE/LoxP recombination, leaving behind one of the LoxP sites.

(D) PCR genotyping. Transfected iPSC clones were screened for correct donor plasmid location (left gel), resulting in 2 kb product (red arrow; primer pair 4) and for exon 9 deletion (right gel) resulting in 2.1 kb product if the deletion is still present (red arrow; primer pair 7) and no product in the absence of deletion. Clones with correct plasmid location without the exon 9 deletion were chosen.

(E) PCR genotyping. Clones were screened for heterozygous repair of the exon 9 deletion allele (left gel), resulting in 0.8 kb product when the healthy allele remained intact (red arrow; primer pair 6). Successful CRE-recombination (right gel) was confirmed with primer pair 8, resulting in 1 kb product when successful (red arrow) or 2.5 kb product when unsuccessful (blue arrow). Clones with intact healthy allele and successful removal of puromycin-resistance cassette were chosen.

(F) Confirmation of the exon 9 inclusion in isogenic control lines at the transcript level. PCR products were amplified from cDNA. The correct product from exon 8 to exon 10 results in a 360 bp band (blue arrow) when the exon 9 is included and in a 273 bp band (red arrow) without exon 9. Control lines and isogenic control lines show only one band of 360 bp whereas AD lines show both bands as a sign of heterozygous deletion of exon 9.

Figure S2

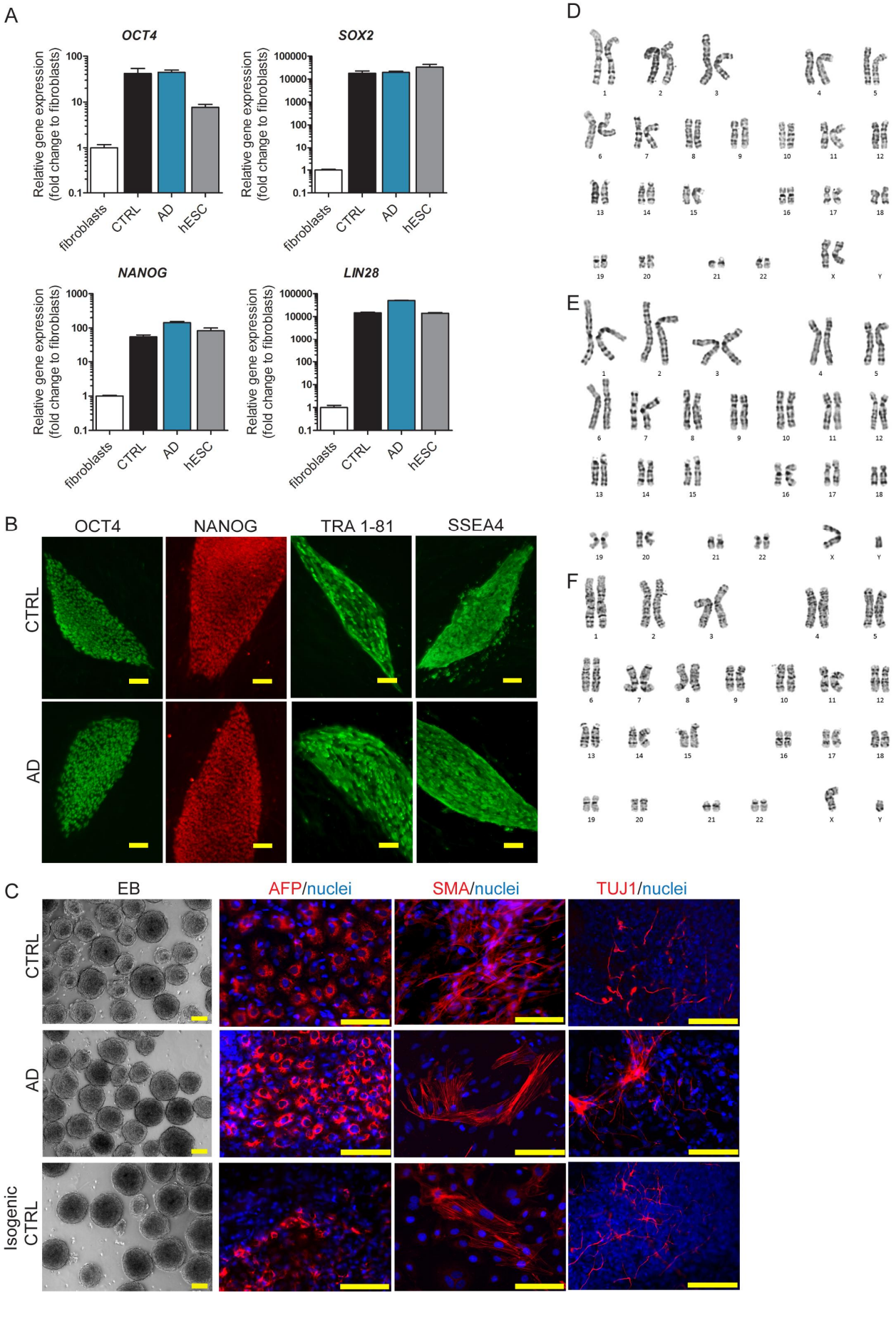
A
OCT4
SOX2
NANOG
LIN28
Relative gene expression (fold change to fibroblasts)
fibroblasts
CTRL
AD
hESC
B
OCT4
NANOG
TRA 1-81
SSEA4
CTRL
AD
C
EB
AFP/nuclei
SMA/nuclei
TUJ1/nuclei
CTRL
AD
Isogenic CTRL
D
E
F

Figure S2. Characterization of iPSC lines. Related to Table 1, Table S1 and all the Figures.
(A) Relative gene expression levels of *OCT4*, *SOX2*, *NANOG* and *LIN28* shown as fold change to fibroblasts. Representative data from one control (Ctrl3) and one AD patient (AD2) are shown. Fibroblasts are included as negative control and HS306 embryonic stem cells (hESCs) as positive control. Data are presented as mean ± SEM.
(B) Representative immunocytochemistry images of OCT4, NANOG, TRA 1-81 and SSEA4 from one control line and one AD line grown on human foreskin fibroblast feeders. Scale bars 100 μm.
(C) Representative bright field images of embryoid bodies (EB) grown in suspension for two weeks and representative immunocytochemistry images of alpha-fetoprotein (AFP, endoderm; red), smooth muscle actin (SMA, mesoderm; red) and beta III tubulin (TUJ1, ectoderm; red) from one control, one AD and one isogenic control line. Nuclei are stained with Hoechst. Scale bars 100 μm.
(D-F) Representative karyograms from one control (D), AD (E) and isogenic control (F) iPSC line showing normal euploid karyotypes (46,XX for D and 46, XY for E and F).
See also Table S1.

Figure S3

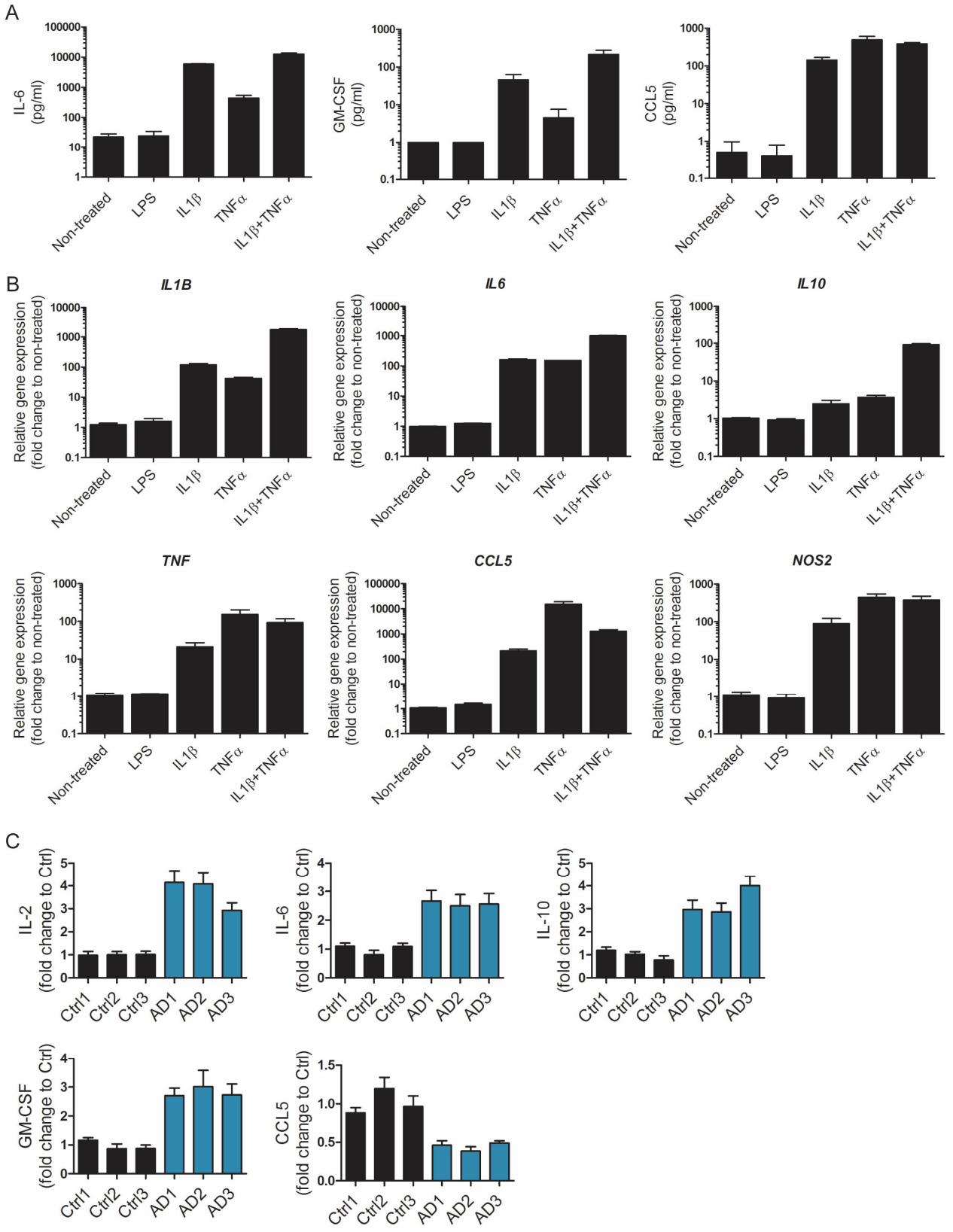
A
IL-6 (pg/ml)
GM-CSF (pg/ml)
CCL5 (pg/ml)
Non-treated
LPS
IL1β
TNFα
IL1β+TNFα
B
IL1B
IL6
IL10
TNF
CCL5
NOS2
Relative gene expression (fold change to non-treated)
C
IL-2 (fold change to Ctrl)
IL-6 (fold change to Ctrl)
IL-10 (fold change to Ctrl)
GM-CSF (fold change to Ctrl)
CCL5 (fold change to Ctrl)
Ctrl1
Ctrl2
Ctrl3
AD1
AD2
AD3

Figure S3. Cytokine profiles of iPSC-derived control astrocytes after different proinflammatory stimuli. Related to Figure 1 and Figure 4.

(A) Astrocytes were either left untreated or treated with 1 µg/ml LPS, 10 ng/ml IL1β, 50 ng/ml TNFα or a combination of IL1β and TNFα for 48 hours. Media was analyzed with CBA assay for the concentrations of secreted IL-6, GM-CSF and CCL5. Representative data from one control line are shown. Data are presented as mean ± SEM from two independent experiments.

(B) Relative gene expression levels of *IL1B*, *IL6*, *IL10*, *TNF*, *CCL5* and *NOS2* after 48 hours of treatment with 1 µg/ml LPS, 10 ng/ml IL1β, 50 ng/ml TNFα or a combination of IL1β and TNFα shown as fold change to untreated cells. Representative data from one control line are shown. Data are presented as mean ± SEM from two independent experiments.

(C) Quantification of IL-2, IL-6, IL-10, GM-CSF and CCL5 concentrations in the media after stimulation with TNFα (50 ng/ml) and IL1β (10 ng/ml) for 48 hours, using CBA assay. Results from individual donors are shown as fold change to control lines (Ctrl1, Ctrl2, Ctrl3). Data are presented as mean ± SEM from three independent experiments

Figure S4

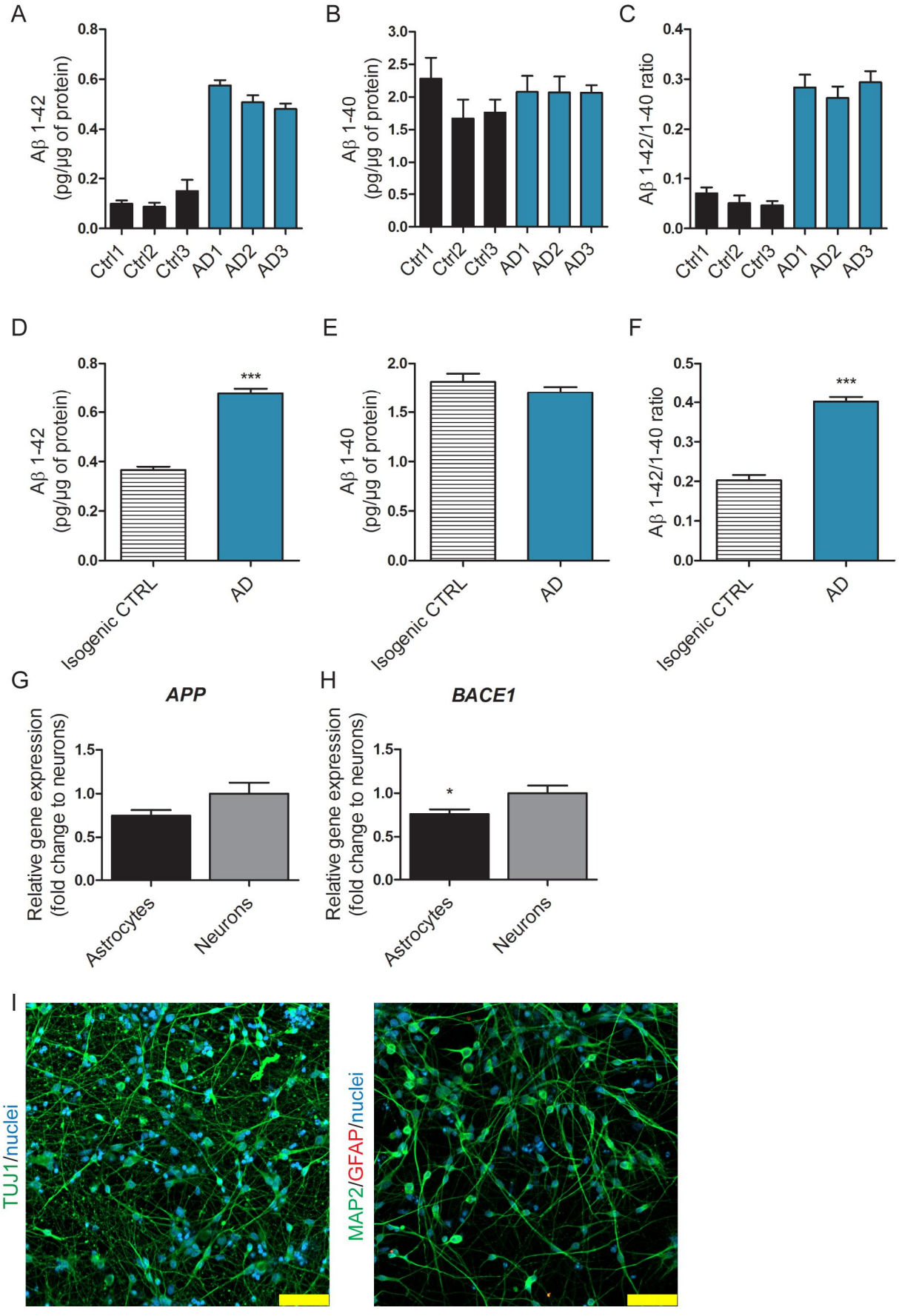
A
Aβ 1-42 (pg/µg of protein)
0.8
0.6
0.4
0.2
0.0
Ctrl1
Ctrl2
Ctrl3
AD1
AD2
AD3
B
Aβ 1-40 (pg/µg of protein)
3.0
2.5
2.0
1.5
1.0
0.5
0.0
C
Aβ 1-42/1-40 ratio
0.4
0.3
0.2
0.1
0.0
D
***
Isogenic CTRL
AD
E
F
G
APP
Relative gene expression (fold change to neurons)
1.5
1.0
0.5
0.0
Astrocytes
Neurons
H
BACE1
*
I
TUJ1/nuclei
MAP2/GFAP/nuclei

Figure S4. *PSEN1 ΔE9* astrocytes and neurons have similar amyloidogenic properties. Related to Figure 2.
(A-C) Aβ 1-42 (A), Aβ 1-40 (B) and Aβ 1-42/1-40 ratio (C) were quantified from conditioned media (72 hours) and normalized to total protein content. Results are shown for individual donors as mean ± SEM from three independent experiments.
(D-F) Amounts of Aβ 1-42 (D), Aβ 1-40 (E) and Aβ 1-42/1-40 ratio (F) were quantified from conditioned media (72 hours) of iPSC-derived neurons matured for two weeks, with ELISA, and normalized to total protein content of each well. Data are presented as mean ± SEM from two isogenic pairs. (n=3 independent experiments, *** $p<0.001$)
(G) Relative gene expression levels of *APP* in matured astrocytes and neurons shown as fold change to iPSC-derived neurons. Data are presented as mean ± SEM. (Astrocytes n=14 lines, neurons n=9 lines)
(H) Relative gene expression levels of *BACE1* in matured astrocytes and neurons shown as fold change to iPSC-derived neurons. Data are presented as mean ± SEM. (Astrocytes n=14 lines, neurons n=9 lines, * $p<0.05$)
(I) Characterization of iPSC-derived neuronal cultures after 2 weeks of maturation. Representative immunocytochemistry images showing beta III tubulin (TUJ1; green) and MAP2 (green) positive neurons. GFAP (red) positive astrocytes were not detected. Nuclei were stained with Hoechst. Scale bars 50 µm.

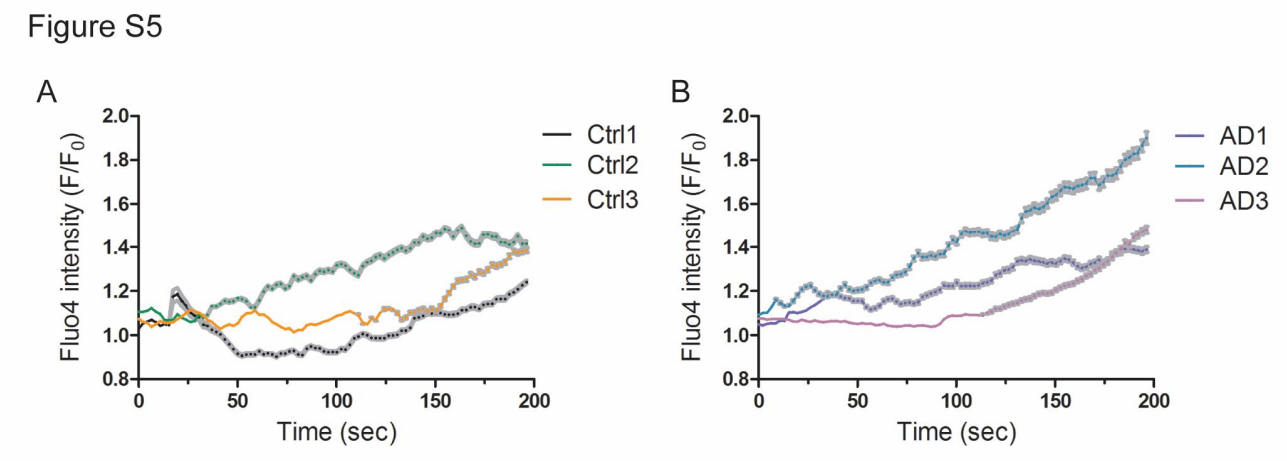

Figure S5. *PSEN1 ΔE9* astrocytes show increased Ca^{2+} leakage from the ER. Related to Figure 3.
(A) Average traces of control astrocytes from individual donors in the presence of 50 µM ryanodine, 100 µM 2APB and 1 µM thapsigargin. Results are shown as mean ± SEM (in gray). (Ctrl1 n=260, Ctrl2 n=289 and Ctrl3 n=265)
(B) Average traces of AD astrocytes from individual donors in the presence of 50 µM ryanodine, 100 µM 2APB and 1 µM thapsigargin. Results are shown as mean ± SEM (in gray). (AD1 n=157, AD2 n=274, AD3 n=109)

Table S1. Summary of the characterizations of iPSC lines used in this study. Related to Table 1 and all Figures.

iPSC line	Reprogramming method	Morphology	Pluripotency gene expression[a]	Pluripotency protein expression[b]	EB formation	Three germ layers[c]	Karyotype	Reference
Ctrl1A	SeV 1.0	+	+	+	+	+	normal	[d] (UEF-2B)
Ctrl1B	SeV 1.0	+	+	+	+	+	normal	[d] (UEF-2C)
Ctrl2A	Lenti	+	+	+	+	+	normal	[d] (UEF-3A)
Ctrl2B	SeV 1.0	+	+	+	+	+	normal	[d] (UEF-3B)
Ctrl3A	SeV 1.0	+	+	+	+	+	normal	This paper
Ctrl3B	SeV 1.0	+	+	+	+	+	normal	This paper
AD1A	SeV 1.0	+	+	+	+	+	normal	This paper
AD1B	SeV 1.0	+	+	+	+	+	normal	This paper
AD2A	SeV 2.0	+	+	+	ND	ND	normal	This paper
AD2B	SeV 2.0	+	+	+	+	+	normal	This paper
AD2B iso	-	+	ND	ND	+	+	normal	This paper
AD3A	SeV 2.0	+	+	+	+	+	normal	This paper
AD3B	SeV 2.0	+	+	+	ND	ND	normal	This paper
AD3B iso	-	+	ND	ND	+	+	normal	This paper

[a] Expression levels of *OCT4, SOX2, NANOG* and *LIN28* by qRT-PCR

[b] Expression of OCT4, NANOG, TRA 1-81 and SSEA4 by immunocytochemistry

[c] Expression of AFP (endoderm), SMA (mesoderm) and TUJ1 (ectoderm) by immunocytochemistry

[d] These lines have been previously characterized in Holmqvist et al., 2016

ND: not determined, EB: embryoid body

SUPPLEMENTAL EXPERIMENTAL PROCEDURES

Generation of isogenic control lines using CRISPR/Cas9. Related to Experimental procedures.
SgRNA pair was identified using the crispr.mit.edu design tool (sequences listed below) and the sgRNA sequences were cloned into a Cas9 sgRNA plasmid (Addgene #68463). The PL552 donor plasmid (Addgene #68407) with 1 kb homology arms, was designed to restore an approximately 700 bp fragment containing exon 9 and the immediately-flanking intronic sequence (350 bp on the 5' end of exon 9 and 250 bp on the 3' end of exon 9) of the full 4.6-kb deletion. Between the 3' intronic sequence and the 3' homology-directed repair arm is a LoxP-flanked PGK-puromycin resistance cassette to facilitate the selection of cells exhibiting HDR at the *PSEN1* locus. The hCas9_D10A plasmid was from Addgene (#41816).
Electroporations were performed using the Neon Transfection System (Invitrogen). iPSCs were cultured in E8 media on Matrigel coated plates and treated with 0.5 µM ROCK-inhibitor for 24 hours prior to electroporation. Cells were harvested with 0.5 mM EDTA, resuspended at $2x10^6$/100 µl, mixed with plasmid cocktail (6 µg hCas9_D10A, 10 µg donor, 2 µg each sgRNA), electroporated (1100 V, 20 ms and 2 pulses) and re-plated on Matrigel in E8 media with 5 µM ROCK-inhibitor. When colonies started to emerge (after 3-4 days), cells were treated with puromycin (0.25 µg/ml, Gibco) for 48-72 hours. Surviving cells were cultured in E8 media until colonies were of sufficient size for picking.
To remove the floxed PGK-puromycin resistance cassette, cells were treated with 10 µl of recombinant TAT-CRE recombinase (Millipore) in E8 media for 20 minutes at 37°C after which the cell were cultured as usual.
Genomic DNA was isolated using QuickExtract DNA Extraction Solution 1.0 (Epicentre).
PCR amplifications were performed using either Q5 high-fidelity polymerase (New England Biosystems) or Phusion high-fidelity polymerase (Thermo Scientific).
Sanger sequencing of the plasmids was performed at Quintara Biosciences and sequencing of the iPSC clones at the Genome Center of Eastern Finland.

Table of SgRNAs and primers used in the generation and screening of isogenic control lines.

Primer pair	Target	Sequence
	sgRNA 1A	TTTTCTATCAGGTTTACTAGTGG
	sgRNA 1B	GGAAAGAATTGCCACAAGCCTGG
1	5' homology arm (cloning)	F: GAAGTGGTTCACTCTGGGAGC R: CCCAGCCTGTTTATGGATTTCC
2	3' homology arm (cloning)	F: GGCCGCTGCTGCCATCAAGA R: TCTTCCTGTCTTCCCAGTGCCATA
3	Exon 9 donor (cloning)	F: TCACCATCTGAGGCTTTTGTGA R: ACCTTTCCATGCTGGTATTCTGT
4	5´ location confirmation	F: GCAAAATGCTCTTACTGACAGG R: ACCCGGTAGAATTTCGAGGT
5	3´ location confirmation	F: GGGAGGATTGGGAAGACAAT R: AGCATGCTCATTGTGCCATA
6	Intact normal allele	F: TCGCTGGTGGCTTCATTTCC R: GCAGCAAGCTGAGTCCAATC
7	Exon 9 deletion	F: GAAGTGGTTCACTCTGGGAGC R: TCTTCCTGTCTTCCCAGTGCCATA
8	CRE-removal confirmation	F: TCACCATCTGAGGCTTTTGTGA R: ACCTACATGCTCACAGACAATCA
9	Whole targeted area for sequencing	F: GCAAAATGCTCTTACTGACAGG R: ATGCTCATTGTGCCATAACTTG
10	Exons 8-10 at transcript level	F: GTGGCTGTTTTGTGTCCGAA R: TCCCATTCCTCACTGAACCC

Quantitative RT-PCR
RNA was extracted by RNeasy Mini Kit (Qiagen) followed by cDNA synthesis with Maxima reverse transcriptase (Life Technologies), or with TaqMan® Gene Expression Cells-to-C_T™ Kit (Applied Biosystems). The mRNA expression levels were determined by quantitative RT-PCR (StepOne Plus™ Real-Time PCR system; Life Technologies) using TaqMan assay mixes (Life Technologies) listed below. Expression levels were normalized to β-Actin (ACTB; Applied Biosystems) using Q-gene program (Equation 2).

Table of TaqMan assay mixes used for mRNA expression studies.

OCT4	Hs00742896_s1
NANOG	Hs02387400_g1
SOX2	Hs01053049_s1
LIN28	Hs00702808_s1
GFAP	Hs00909233_m1
S100B	Hs00902901_m1
SLC1A2	Hs01102423_m1
SLC1A3	Hs00188193_m1
AQP4	Hs00242342_m1
IL1B	Hs01555410_m1
IL6	Hs00985639_m1
IL10	Hs00961622_m1
TNF	Hs99999043_m1
CCL5	Hs00982282_m1
NOS2	Hs01075529_m1
APP	Hs00169098_m1
BACE1	Hs01121195_m1

Immunocytochemistry

Cells were fixed with 4% paraformaldehyde and stained as previously described (Puttonen et al., 2013). Primary antibodies and dilutions are listed in Supplemental experimental procedures. Alexa Fluor 488 or 568 conjugated secondary antibodies (1:500, Thermo Fisher Scientific) were used for detection and nuclei were counterstained with Hoechst 33258 (Sigma).

Table of primary antibodies used for immunocytochemistry.

Target	**Dilution**	**Source**	**Catalog number**
OCT4	1:400	Chemicon	MAB4401
NANOG	1:100	R&D Systems	AF1997
TRA 1-81	1:200	Chemicon	MAB4381
SSEA4	1:400	Chemicon	MAB4304
AFP	1:500	Sigma	A8452
SMA	1:500	Sigma	A5228
TUJ1	1:2000	Covance	MMS-435P
GFAP	1:500	Dako	Z0334
S100β	1:1000	Abcam	ab11178
MAP2	1:400	Chemicon	MAB3418

Embryoid body assay

For embryoid bodies (EBs), iPSC colonies were mechanically lifted from Matrigel plates and cultured in suspension for 2 weeks using ultra-low attachment plates (Corning). The EBs were plated down on matrigel-coated coverslips to allow outgrowth of differentiated cells for 2 weeks. Media (1:1 mixture of E8-medium and ES-medium without bFGF) was changed every 2-3 days.

Karyotyping

iPSCs were arrested with 200 ng/ml KaryoMAX® Colcemid™ Solution (Invitrogen) and harvested. Karyotyping was performed at the Eastern Finland Laboratory Centre Joint Authority Enterprise (ISLAB, Kuopio, Finland) using Giemsa (G-banding) staining. A total of 20 metaphase cells were analyzed per line.

Western blotting

Western blotting was done as previously described (Viswanathan et al., 2011) with the following antibodies and dilutions: PS-1 (MAB5232, 1:1000; Chemicon), APP (A8717, 1:2000; Sigma) and GAPDH (ab8245, 1:15 000; Abcam).

Neuronal differentiation

Neuronal differentiation was carried out similarly to astroglial differentiation (described in the Experimental methods) until the neural progenitor sphere stage. To support neuronal enrichment, spheres were maintained in NDM media supplemented with 0.5 IU/ml heparin, 20 ng/ml bFGF and 10 ng/ml EGF. For neuronal maturation, spheres were dissociated with Accutase and plated on to poly-l-ornithine/Matrigel-coated dishes in NDM supplemented with 10 ng/ml BDNF and 10 ng/ml GDNF (both from Peprotech).

SUPPLEMENTAL REFERENCES

Puttonen, K.A., Ruponen, M., Kauppinen, R., Wojciechowski, S., Hovatta, O., and Koistinaho, J. (2013). Improved method of producing human neural progenitor cells of high purity and in large quantities from pluripotent stem cells for transplantation studies. Cell Transplant *22*, 1753-1766.